Aus dem International Graduate Program Medical Neurosciences der Medizinischen Fakultät Charité – Universitätsmedizin Berlin

DISSERTATION

Novel Oblique Plane Microscopes for Whole-Brain Imaging of Danionins

zur Erlangung des akademischen Grades

Doctor of Philosophy (PhD)

vorgelegt der Medizinischen Fakultät
Charité – Universitätsmedizin Berlin

von

Maximilian Hoffmann

aus Halle (Saale)

Datum der Promotion: 26.06.2022

Contents

Zusammenfassung

Die gleichzeitige Messung neuronaler Aktivität von Nervenzellen im ganzen Gehirn oder Nervensystem würde es ermöglichen Eigenschaften und Dynamik von ausgedehnteren neuronalen Netzwerken zu untersuchen. Optische Messung neuronaler Aktivität mit Hilfe von genetisch expremierten Kalziumindikatoren ist hier eine attrakive Methode, da sie erlaubt Neuronen in einem größerem Bereich aufzunehmen. Allerdings ist dieser Bereich durch Lichtstreuung im Gewebe und technische Limitierungen begrenzt.

In Tiermodellen, wie Zebrabärblingslarven, juvenilen Zebrabärblingen (*Danio Rerio*) und *Danionella translucida* (DT), ist die Messung gehirnweiter neuronaler Aktivität mittels optischer Methoden prinzipiell dennoch möglich, da diese klein und transparent sind. Allerdings erlauben es gegenwärtig existierende Mikroskope nicht die Vorteile dieser Tiermodelle auszuschöpfen, da dies ein optimiertes Ausbalancieren von Auflösung, Aufnahmerate und Sichtfeld erfordert.

Einzelobjektiv-Lichtblattmikroskopie (engl. Oblique Plane Microscopy, OPM) ist eine Mikroskopietechnik, die potentiell dazu geeignet ist dies zu leisten. Allerdings war diese Technik bisher auf die Nutzung eines Objektivs mit hoher numerischer Apertur (NA) angewiesen. Dies begrenzte ihr Sichtfeld auf einen Durchmesser von ca. 1mm, welches kleiner als das ganze Nervensystem eines juvenile Zebrafischbärblings oder das Gehirn von DT ist.

Im Rahmen dieser Arbeit entwickelte ich daher eine Familie von Einzelobjektiv-Lichtblattmikroskopen, die dieser Beschränkung nicht unterliegen. *Diffractive Oblique Plane Microscopy* (DOPM) und *Image Transfer Oblique Plane Microscopy* (IOPM) operieren bei niedriger und mittlerer numerischer Apertur und sind daher in der Lage innerhalb eines Sichtfelds von 3.3 mm × 3.0 mm × 1.0 mm und 2 mm x 1.4 mm x 1 mm (XYZ) abbzubilden.

Ich zeige, dass DOPM in der Lage ist das gesamte Nervensystem eins juvenilen Zebrafischbärblings mit der Rate von einem 1Hz aufzunehmen und es erlaubt neuronale Aktivität von großen Teilen des Gehirns zu messen. Weiterhin zeige ich, dass IOPM es ermöglicht simultan neuronale Aktivität im ganzen Gehirn einer ausgewachsenen DT aufzunehmen und es somit erlaubt Charakterstika des gesamten auditorischen Systems zu ermitteln.

Die aus diesen Entwicklungen resultierende Möglichkeit, gehirnweite neuronale Aktivität von juvenilen Zebrafischbärblingen und ausgewachsenen DT mit hoher Geschwindigkeit zu messen, wird es ermöglichen neue Einsichten in die Funktionsweise von gehirnweiten neuronalen Netzen und dem Zusammenwirken unterschiedlicher Gehirnareale zu ermöglichen.

Abstract

The ability to simultaneously monitor the neural activity distributed throughout the entire brain would enable scientists to address complex questions related to how neural activity is organized across neural circuits.

Optical imaging with the help of genetically encoded calcium sensors promises to bring this goal within reach, but the optical access is limited by scattering of the biological tissue and optical engineering constraints.

Fortunately, non-human animal models such as *Danionella translucida* (DT) and the larval or juvenile *Danio Rerio* (zebrafish) are small and transparent throughout their life. Optical imaging studies of these organisms therefore are ideally suited to monitor brain-wide neural activity. However, existing microscopy systems do not take full advantage of the potential of these animal models, which would demand an optimized trade-off between resolution, speed, and field of view (FOV).

Oblique plane microscopy (OPM) is a technique that potentially is able to overcome these limitations. So far, these techniques have relied on the use of high numerical aperture (NA) detection objective lenses, limiting their FOV to around 1 mm x 1 mm, which is too small to accommodate the nervous system of juvenile zebrafish or the brain of adult DT.

I addressed this limitation by designing, building and characterising a family of new OPM variants, diffractive oblique plane microscopy (DOPM) and image transfer oblique plane microscope (IOPM), which have a significantly larger FOV. They operate at low and intermediate NA therefore achieve a FOV of 3.3 mm × 3.0 mm × 1.0 mm and 2 mm x 1.4 mm x 1 mm, respectively.

I show that DOPM can be used to image the whole nervous system of a juvenile zebrafish at 1Hz and it allows us to extract neural signals from large parts of its brain. Furthermore I show that IOPM is able to simultaneously record neural activity throughout the whole brain of an adult DT at 1Hz and allows us to map out features of the whole auditory pathway of DT.

The resulting ability to simultaneously record neural activity throughout the whole brain of juvenile zebrafish and the adult DT at an unprecedented speed will enable us to advance our understanding of the functioning of brain-wide circuits and the complex interplay of different brain areas in vertebrates.

1 Introduction

1.1 Understanding the Nervous System through Neural Population Imaging

The aim of modern neuroscience is to build an understanding of the nervous system of animals. It therefore touches upon question that are already millennia old, such as the difference between animate and inanimate nature, the causes and rules that produce the behavior of animals and the properties of mental phenomena and perception.

Modern neuroscience approaches these questions by using the scientific method. One hallmark of the scientific method is the controlled and selective gathering of observations and measurements from the systems that are to be understood. If possible, additional causal interventions accompany these measurements and constitute the scientific experiment. This makes advances in scientific understanding of the world equally dependent on theoretical insights, methodological innovations, and a careful selection of the system to be studied.

Throughout its history, neuroscience has therefore progressed through method developments, such as the staining methods by Camillo Golgi [1], the careful selection of experimental systems, such as sea slug Aplysia by Eric Kandel [2], and conceptual insights, such as the predictive coding hypothesis developed by Horace Barlow [3].

These innovations have led up to the contemporary understanding of the nervous system as an interconnected cellular network of thousand to billions of neurons. Within this network, the membrane potential of each neuron can be changed via neurotransmitters released at chemical synapses, neuromodulators in the extracellular space, or direct electrical coupling with neighboring cells via gap junctions. Upon crossing a threshold, this change in membrane potential leads to action potentials, milliseconds long rapid all-or-nothing jumps in membrane voltage. The action potentials are transmitted along thin projections, the axons, and lead to the release of neurotransmitters at the synapses located at the axon terminals. At the synapses the neurotransmitters in turn lead to an increase (excitatory connection) or decrease (inhibitory connections) in membrane potential of the connected post-synaptic cells [4].

At a high level of abstraction the brain can therefore be conceptualized as a dynamical or information processing system consisting of many recurrently coupled non-linear units, that change their membrane potential over timescales of milliseconds [5]. This system causes the behavior of the animal via efferent projections to the neuro-muscular junction and is affected by changes in its surrounding via afferent projections from sensory organs and internal processes of the organism [4].

One great achievement of modern systems neuroscience is the discovery that information about the behavior of the animal can, in some settings, be decoded from a recording of only a subset of the neurons in the brain [6, 7]. Additionally, neural activity of such population recordings is often found to be low dimensional in nature [8]. It is currently unknown, whether the recorded neural activity will remain low dimensional, if more neurons in distant areas are recorded simultaneously during more complex and natural behaviors.

Since neural activity related to behavioral markers like locomotion or thirst can be found throughout the whole brain [9, 10], it is plausible that cognitive phenomena and neural processes involve many neurons distributed throughout distant brain areas. To understand the internal functional building blocks and principles of the nervous system will therefore require measurements of large parts of the ongoing activity in a large number of neurons (thousands to billions) across the entire brain. The ability to do so depends on the availability of appropriate measurement tools, as well as on the choice of a suitable nervous system, to which they can be applied.

1.2 The Instruments

From the middle of the 20th century until today the number of neurons that can be recorded simultaneously has steadily increased from a single neuron to thousands of neurons [11]. This advancement in what we can measure within the living brain was achieved using a variety of technologies, the most prominent of which are shown in Figure 1.

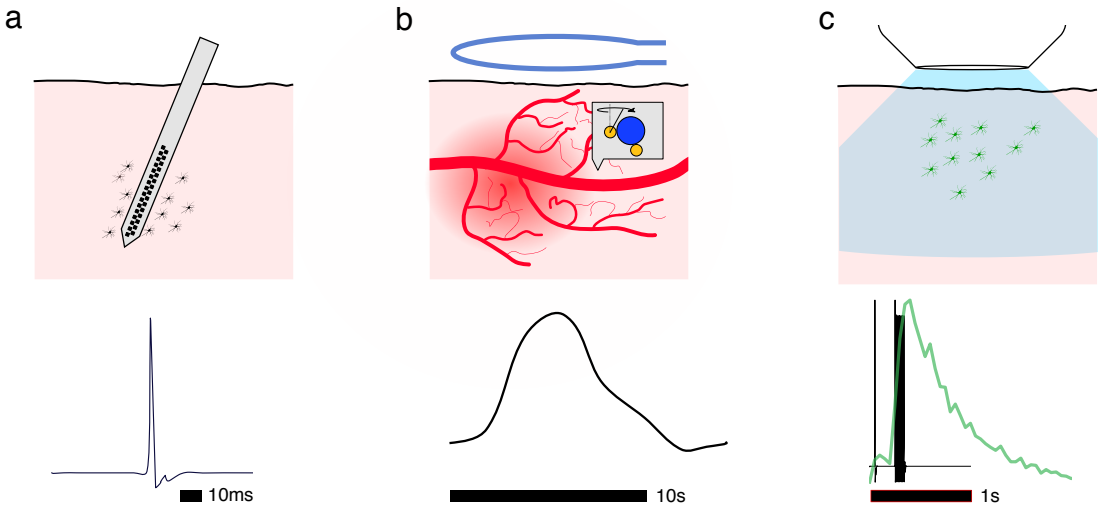

Figure 1: Three Common Methods for Recording Neural Activity - *The upper panel shows a simplified recording scheme, whereas the lower panel shows the temporal properties of the measured signals: (a) Electrical Recordings – a probe consisting of multiple independent recording channels is inserted into the nervous tissue. If cells fire action potentials, corresponding voltage changes are measured at multiple channels at a kHz rate. The temporal resolution allows to record single action potential. (b) Functional Magnetic Resonance Imaging (fMRI) – Local oxygen consumption of the nervous system can be measured via resonance of nuclear spin in an external magnetic field. This signals serves a proxy for the total neural activity of a population of neurons and has a temporal resolution of 1 to 2 seconds. (c) Optical Neural Imaging with Calcium Indicators – Neurons are filled with a calcium indicator, or genetically modified in order to express the calcium indicator. Action potentials fired by a neuron lead to a change in fluorescence with a specific rise (tens of milliseconds) and fall time (hundreds milliseconds) depending on cell type and calcium indicator. This signal has to be recorded by an optical system for as many neurons as possible and can then be turned into time series data. Illustration by Maximilian Hoffmann*

Electrical Recordings

The oldest and most direct method to measure neural activity is to place an electrode into the nervous tissue and measure the local voltage, which carries information about the spiking activity of nearby neurons [12]. Initially a single electrode was used to record from one or two neurons [13, 14]. Starting in the 1970s the development of multi-electrode setups and electrode arrays gradually allowed to increase this number to tens to hundred of neurons [15]. Today, the most recent electrical recording technology is a 100 µm thick and 1 cm long probe, along which 936 recording channels are placed. This so-called Neuropixel probe [16] can locally record electrical signals of thousands of neurons at temporal resolution of up to 10 kHz, where single action potentials can be tracked (Figure 1a).

Despite its superb temporal resolution electrical recording of neural activity has limitations. Electrical recordings of neuronal activity are only possible from neurons in spatial proximity of the recording electrode and do not reveal their accurate spatial locations. Additionally, recording distributed circuits across multiple brain regions is often difficult, as not all regions that comprise the circuit can be reached with one or even multiple probes at the same time. Finally the nervous tissue has to be able to tolerate the incision and tissue displacement caused by the probe. For smaller animals, which are themselves only on the order of hundreds of micrometer, an insertion of a multichannel probe is therefore often not possible.

Functional Magnetic Resonance Imaging

Functional magnetic resonance imaging (fMRI) is a non-invasive method to measure neural activity, established during the 1990s. Here the tissue is excited with a radio-frequency pulse and the subsequent resonant behavior of the nuclear spin of water protons in an external magnetic field is measured. Increased neural activity locally changes the vascular concentration of paramagnetic deoxy-hemoglobin, which changes the measured resonance behavior [17, 18]. This blood-oxygen-level-dependent (BOLD) contrast then serves as an indirect measure of neural activity.

fMRI in its current form can reach a spatial resolution of $\sim$1 mm^3 and its temporal resolution is limited by the dynamics of cerebral blood flow to $\sim$1-2 s [18]. While the recording volume is large and allows for imaging of the entire human brain the fMRI signal is merely a proxy for the average activity of thousands of cells due to low spatial resolution. Therefore neural signals can be located throughout a vast volume, yet neural activity in a population of neurons cannot be followed with cellular resolution (Figure 1).

Optical Recording Of Neural Activity

Another approach is to optically measure activity with the help of a microscope. Microscopy has long played a role in neuroscience research for neuroanatomy and cell morphology. The immense utility of microscopy has become more apparent only through the development of contrast mechanisms, which allowed researchers to selectively mark constituents of the otherwise largely transparent nervous tissue. The oldest contrast mechanism is the staining of

a subset of cells by marking them with absorptive dye, as developed by Camillo Golgi in the 1870s [1]. Since then other contrast methods have been developed. Some are intrinsic, such as differential interference microscopy [19, 20], and make use of the phase modulation that light undergoes while passing through the inhomogeneous tissue, whereas others rely on the selective modification of the specimen in order to create optical contrast.

An ubiquitously used application of the latter approach in contemporary neuroscience is fluorescence microscopy [21]. Here the contrast is achieved with help of fluorescence. A molecule undergoes fluorescence, when it is excited by a photon at one wavelength and after relaxation into a lower electronic state state emits a photon at a larger wavelength [22]. Materials that exhibit fluorescence can be artificially synthesized, but also occur naturally, and in animals and plants such as in the case of the Green Fluorescent Protein (GFP), originally isolated from the jellyfish Aequorea Victoria [23]. These molecules can be delivered into nervous tissue, but also genetically expressed in selective cells via insertion of the suitable DNA construct into the organism [24]. The labeled structures will then emit light of a certain color, i.e. green (520nm) in the case of GFP, upon excitation by their excitation wavelength, i.e. 488 nm in the case of GFP [23].

Given its usefulness for investigating the anatomical structure of the nervous system it is a natural question whether optical techniques can also be used to measure electrical activity in neurons. Indeed early experiments showed that even intrinsic optical properties of nervous tissue are correlated with neural activity. However the possibility to derive scientific insights from these measurements *in vivo* were limited as they are either not highly localized [25] or suffer from a very low signal-to-noise ratio [26]. The development of synthetic fluorescent calcium indicator molecules [27] overcame these limitations and presented a great step towards making optical neuroimaging possible (Figure 1c) [28, 29].

These fluorescent molecules change the efficiency of the conversion of excitation into emission light, the excitation cross-section, and therefore their brightness, depending on the local calcium concentration. The intracellular calcium concentration in turn is a proxy for the neural action potential since any single action potential will lead to the opening of voltage gated calcium channels causing an influx of calcium into the cell [30, 31]. Upon excitation of the fluorescent calcium indicators, the emitted fluorescence will therefore be correlated to the membrane voltage of the cell. Further research led to development of calcium sensor proteins that are based on GFP. These indicators can be genetically expressed and therefore do not have to be delivered to the organism [32, 31]. This is advantageous since permanent integration into the genome allows for chronic and minimally invasive labelling of genetically defined large neural populations.

At the cellular level, the two factors that determine the temporal dynamics of the signal of both the synthetic and genetically encoded calcium indicators are the dynamics of the calcium flux following an action potential and the kinetics of the indicator molecule. The fluorescence signal caused by a single action potential therefore typically has a rise time of 50 to 500 ms and a decay time of up to a few seconds [33].

The number of neurons and the quality of the recorded signal depends on the imaging volume

of the microscope as well as the accuracy and speed with which this fluorescence signal can be recorded and attributed to neural loci. Although the resolution of optical systems can be below one micrometer and therefore small enough to resolve single neurons, it is currently technically challenging to maintain high resolution over imaging volumes larger than a couple of millimeters [21]. Additionally the imaging depth of optical imaging of neural activity is limited by light scattering: Nervous tissue is largely non-absorbing, but nevertheless scatters light on its path through the tissue due to refractive index inhomogeneities. This quickly leads to a deterioration of image quality as the imaging depth increases. It is therefore currently impossible to image deeper then $\sim$1 mm [34].

Despite the temporal resolution and the limit posed by tissue scattering, optical imaging has unique advantages over electrical recordings and fMRI. Electrical recordings of brain activity currently enable recording from thousands of neurons with high temporal and cellular resolution in the immediate vicinity of the probes employed. However the number of probes that can be implemented is limited due to their invasiveness. fMRI recordings are able to non-invasively probe large neural volumes, but only at rather coarse spatial and temporal resolution, and therefore do not permit inference of the neural population activity. Here, optical recording methods stand out with their potential cellular resolution and sub-second temporal resolution. This promises to enable the recording from distributed neural circuits of arbitrary shape as long as they can be accommodated within the field of view (FOV) of the microscope and sampled at a sufficient speed. Therefore, in recent years, multiple microscopy techniques have been introduced that try to extend the limits in which the optical recording of neural activity is possible.

1.3 Microscopy Zoo

The common goals of microscope design for optical neuroimaging of population activity with fluorescence microscopy are to maximize the number of neurons that can be monitored at high temporal resolution. Since engineering design is always a trade-off this has led to a variety of techniques with different advantages as well as technical complexity.

In its simplest form, the epi-fluorescence microscope (Figure 2), the whole sample is excited by a light source, such as a LED or a laser. The time-varying fluorescence of the excited cells can then be recorded by a camera sensor.

Almost all neural circuits occupy an extended volume and it is therefore highly desirable to be able to record this three dimensional information. In the case of epi-fluorescence microscopy, however, it is impossible, because fluorescence is also excited outside the native imaging plane of the microscope (Figure 2, last row). These excited points in different axial planes will quickly de-focus and therefore contribute to background noise at the native focal plane. This problem is commonly referred to as the absence of optical sectioning and for a very densely labeled sample prohibits the imaging of even a single plane. Therefore several microscopy designs have been put forward that try to capture volumetric information and maintain optical sectioning.

The most common microscopy method used for optical neuroimaging *in vivo* is multiphoton point

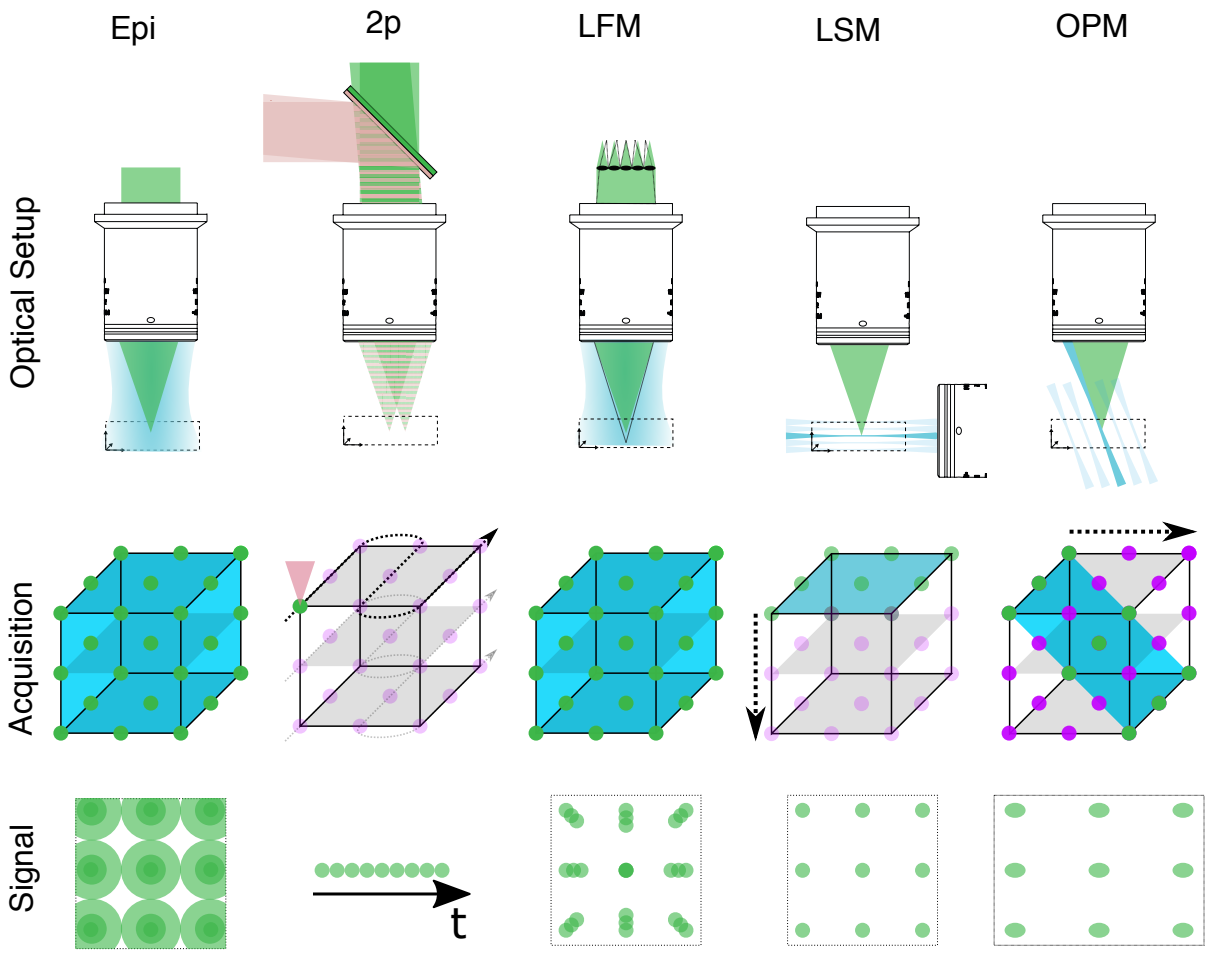

Figure 2: Different Fluorescent Microscope Techniques Used for Optical Recordings of Neural Activity - *For every technique a simplified optical setup (top row), its acquisition scheme (middle row) and its detector/camera image (bottom row) is shown, from left to right: Epi-fluorescence microscopy excites the volume by shining blue light on the whole sample. All imaging points are excited simultaneously and emit fluoroescence (green). Their de-focused images mix on the camera sensor and cannot be discerned. Two photon point scanning microscopy (2P) is imaging one point at a time by non-linearly exciting fluorescence (green) with a scanned laser focus (red). Light field microscopy (LFM) excites and images the whole imaging volume at once by wide field illumination (blue).The image of each point is position dependent. The volumetric information is encoded in a 2D camera image and can be computationally inferred. In light sheet microscopy (LSM) a single plane is excited by creating a thin sheet of light and imaged with an imaging system orthogonal to the excited sheet. The plane can be scanned through the sample and the camera records one plane at a time. In oblique plane microscopy (OPM) these planes are oblique since excitation and emission are recorded through the same objective. OPM is similar to LSM in that it excites and images one plane at a time. However this time both the excitation and the emission are achieved through one objective. Again the created oblique plane can be scanned, in the case of OPM laterally, through the object in order to achieve volumetric imaging. Illustration by Maximilian Hoffmann*

scanning microscopy (Figure 2) [35]. Here a diffraction limited laser focus of a pulsed laser is sequentially scanned through the imaging volume and non-linearly excites fluorescence localized

in a diffraction limited volume around the laser focus. The intensity of the emitted fluorescence from each point is then measured with help of a single pixel detector such as a photo multiplier tube (PMT). The resulting dataset is a time series of fluorescence intensity. Every time point can be attributed to a precise spatial position based on scanning position and due to the confinement of the excitation to a small volume in space and time. Therefore optical sectioning and even resilience to scattering is maintained. With help of this technique large FOVs of up to 5 mm have been achieved [36]. The temporal throughput of any technique can be measured by the number of points or cells that can be recorded per second. In the case of multiphoton point scanning microscopy this throughput currently is limited by sequential scanning scheme of the laser focus. Additionally the fluorescence lifetime puts a fundamental limit on the acquisition rate for multiphoton point scanning microscopy or any sequential microscopy technique: Because the emission of the light after the excitation is on average delayed by several nanoseconds, imaging faster would lead to cross talk between consecutive points.

To circumvent these speed limitations other microscopy techniques employ a parallel detection scheme by recording data from different points at the same time. Some techniques record a whole 3D volume onto a 2D camera in a single exposure by refocusing different axial planes onto different parts of the camera sensor with help of diffractive optical elements [37]. Other, like light field microscopy (LFM), combine multi-aperture imaging with a computational reconstruction (LFM, Figure 2, row 3) [38, 39, 40]. Although these techniques are genuinely volumetric in that they allow the reconstruction of an image volume, they are limited by their lack of optical sectioning: As in the epi-fluorescence microscope these techniques excite fluorophores across the whole imaging volume. The reconstruction of the volume will therefore only be faithful, if the sample is sparse enough.

A family of microscopy techniques which use a parallel detection scheme while maintaining optical sectioning are selective plane illumination or lightsheet microscopes (LSM) [41, 42] (Figure 11. Here planes in the specimen are excited one at a time from the side by a thin sheet of light and then imaged onto a camera sensor. Since the excited fluorophores are confined to a thin region there is no out of focus blur and optical sectioning is maintained. Although LSM still involves sequential scanning, whole 2D planes are recorded simultaneously through the camera sensor, which typically contains millions of pixels. This allows one to record from many cells at the same time and leads to a very high throughput. The 90 degree angle configuration between illumination and imaging system ensures optical sectioning and a high axial resolution, but demands optical access to the sample from two sides, which is often not feasible experimentally.

To enable a similar imaging in the case of limited optical access oblique plane microscopy (OPM), a variant of LSM has been developed. Here oblique planes in the specimen are excited and imaged through one and the same objective. This is possible, because modern imaging objectives with high numerical aperture (NA) can focus light within an angle of almost up to 80 degrees. These objectives can therefore image and excite a plane at the same time while maintaining an angle between the two light paths [43, 44, 45, 46, 47, 48, 49, 50, 51, 52]. Similarly to

LSM, in OPM the volumetric imaging is recorded by sequentially exciting and recording fluorescence in different oblique planes in the specimen. OPM sacrifices the superb axial resolution of two photon point scanning or lightsheet microscopy since the excitation volume is less confined. However it maintains optical sectioning and high throughput due it its confined excitation and parallel detection scheme.

With their different acquistion and detection schemes, microscopy techniques currently used in neuroimaging have diverse limitations. Usually these limitations in resolution, speed and FOV as well as the optical sectioning capability can be traded off against each other, but the degree to which this is possible varies. This in turn implies that the right choice of the microscope will be highly dependent on the question and animal model investigated.

1.4 *Danio Rerio* and *Danionella Translucida*: Animals Suited for Optical Imaging

Optical neuroimaging and the resulting development of new microscope techniques presented above have led to imaging volumes of several cubic millimeters and the recording of neural activity of thousands of neurons [53]. Concurrent to this development of optical methods, novel model organisms were introduced to neuroscience. One example is the teleost zebrafish (*Danio Rerio*) (Figure 3a-c). Zebrafish are particularly suited for imaging studies and larval zebrafish were the first animal, in which *in vivo* optical neuroimaging was performed [29]. Since then, it has become a popular neuroscience model, because of its optical transparency in the larval and juvenile stage, the availability of genetic tools for neurophysiological manipulation, and its relatively small brain [54](Figure 3b).

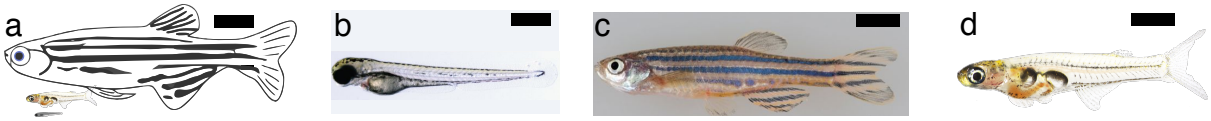

Figure 3: The Danionins Danio Rerio (zebrafish) and Danionella Translucida (DT) - *(a) Illustrations of adult zebrafish, a adult male DT and a larval zebrafish (72 h post fertilization, hpf) side by side, (b) larval zebrafish, 72 hpf , (c) adult zebrafish, (d) male adult DT. Scale bars: (a): 1 cm, (b): 1 mm, (c):1 cm, (d):2 mm, Source: Created by Maximilian Hoffmann, except (b) and (c) adapted with permission from [55]*

This optical transparency combined with the pan-neural expression of the calcium indicator GCaMP enabled to record stimulus triggered response maps at cellular resolution throughout the whole brain of 6 day old larvae (6 days post fertilization (dpf)) using two-photon point scanning microscopy by iteratively recording single planes while the stimulus was repeatedly delivered [56]. Using microscopy techniques such as light sheet microscopy or structured illumination microscopy, with parallel detection schemes, it has since then been possible to record whole brain activity of larval zebrafish at 5 dpf at cellular resolution in a tethered preparation [42] as well as freely moving [57] at a volume rate of 1 Hz. These experimental paradigms led to the unique opportunity to study the brain-wide correlates of motor-adaptation [58], explorative swimming [59], foraging [60], heat perception [57, 61], evidence accumulation [62], and other

behaviors.

As larval zebrafish develop into their adult stage, their behavioral repertoire becomes more complex and includes social behavior such as shoaling and aggression. This is likely accompanied by a maturation and modification of underlying neural circuits and it is therefore desirable to extend imaging studies to juvenile and adult zebrafish. Besides demanding larger FOVs from the microscope, non-invasive imaging in older zebrafish is hampered however by a developing cranium. Starting at the lateral side of the head, the ossification of cartilage progressively leads to a loss of transparency as zebrafish develop into their adult stages [63](Figure 3c).

As a possible alternative, Schulze et. al [64] recently introduced the small transparent teleost fish *Danionella translucida* (DT) as a model organism for neuroscience (Figure 3a,d). Similar to adult zebrafish, DT exhibits a rich behavioral repertoire, such as hunting, schooling, and shoaling. Additionally male DT communicate acoustically by clicks, which are produced by vibrating their swimbladder with a dedicated muscle. Besides having the smallest known vertebrate brain of only 2.5 mm $\times$ 1 mm $\times$ 0.6 mm, and only $\approx$ 650000 neurons, DT also maintains optical transparency throughout its life because it does not develop a dorsal part of the cranium. Hence, adult DT are more amenable to optical imaging than adult zebrafish. Conveniently, due to their phylogenetic proximity, large parts of the existing molecular biological toolkit of zebrafish research can be used to genetically modify DT and therefore express calcium indicators in its neurons.

The appeal of both species, *Danio rerio* and *Danionella translucida*, is the optical accessibility of their whole brain and the potential to simultaneously image distributed neural circuits. In principle this allows for the investigation of neural circuits that take part in the mediation of complex behaviors during development and adulthood by imaging the neural activity throughout the whole brain or even nervous system. This however demands a microscope that is fit for the task.

1.5 Oblique Plane Microscopy for Large Field of Views

Of all microscopy techniques discussed in Section 1.3, oblique plane microscopy (OPM) is the most suitable candidate solution for imaging the whole-brain of small organisms such as DT and juvenile zebrafish. Because of its parallel detection scheme it has a much higher theoretical throughput than two-photon point scanning microscopy and therefore promises to be able to sample the whole-brain at much higher rates. Since it is a light sheet approach, it maintains optical sectioning. However in contrast to LSM it only requires optical access from one side, which is crucial since lateral optical access in our samples is usually occluded by the eyes, thick cartilage or even bones.

The basic excitation geometry of an OPM is again shown in Figure 4. A light sheet is coupled off–axis into the imaging objective and excites an oblique plane within the specimen. This leads to the emission of fluorescence, which can then be captured. However the oblique orientation of the image plane demands a special imaging solution. If one were to place the camera directly

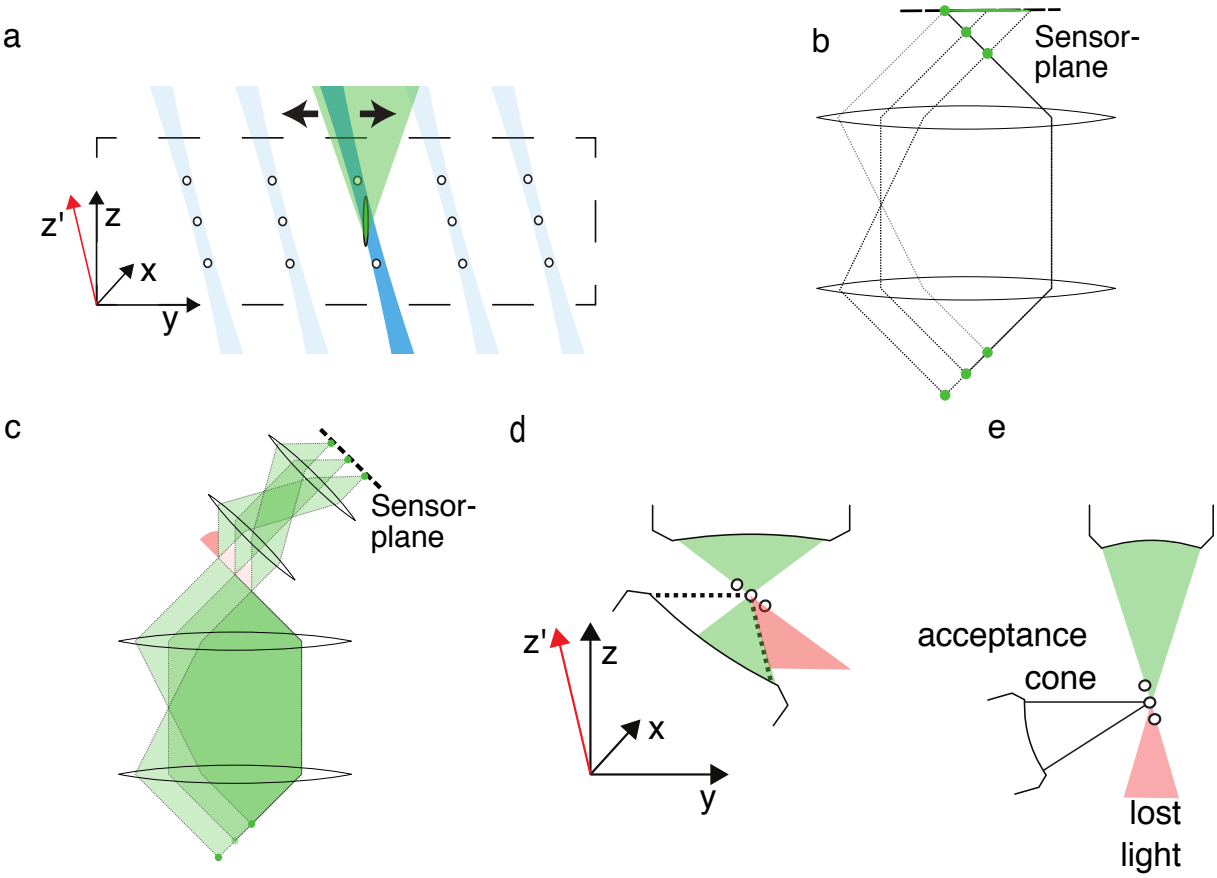

Figure 4: The Re-imaging Step of OPM - *(a) Acquisition geometry of an OPM: an oblique plane is excited by a light sheet and the emitted fluorescence is captured through the same objective. (b) in a 1:1 imaging system the oblique plane is again imaged onto an oblique plane, it is therefore impossible to image this plane onto a straight sensor as in conventional microscopy since large parts of the plane would be out of focus (c) a conventional OPM therefore uses a re-imaging step, in which a tertiary imaging system is re-imaging the oblique plane onto a sensor. (d) However parts of the light are always necessarily lost at this step, (e) as the numerical aperture decreases the fraction of detected light approaches 0 % and therefore this re-imaging solution fails. Illustration by Maximilian Hoffmann*

at the image plane as in a normal microscope, it would either lead to out of focus blur or an inacceptable shallow incidence of the light on the camera chip (Figure 4b).

Therefore a conventional OPM employs an additional re-imaging step to image the plane of interest onto a camera sensor. As shown in Ref. [65] volumetric imaging free of spherical aberrations is possible, if the axial and lateral magnification of an optical system are both uniform. By using such an optical system it is therefore possible to create an aberration-free intermediate image of the excited plane with a uniform magnification. This plane is then brought to lie in the focal plane of a tertiary imaging system, which, now in the geometry of a conventional microscope, images the plane onto a camera sensor with the required magnification (Figure 4c). This conventional re-imaging approach is limited to systems with relatively high NA (Figure 4d), but leads to a total loss of light for systems above NA 0.5 (Figure 4e). Because of this constraint and

the fact that NA and FOV are inversely proportional to date, no OPM exists with a FOV above 600×1000 µm^3 [44]. This size in insufficient for simultaneous imaging of the whole brain of *Danionella translucida* or the whole nervous system of larval and juvenile zebrafish. Therefore the goal of this thesis was to develop new solutions to enable OPM for larger FOVs.

To achieve this, I developed new solutions to the OPM re-imaging step, applicable at low and intermediate NAs, and implemented them by building two custom microscopes. Diffractive oblique plane microscopy (DOPM) presented in Section 2.1 and published in [66] solves the re-imaging problem for low NAs by re-directing the light with help of a diffraction grating, placed at the intermediate image plane. Using this solution my DOPM system, which operates at 0.28 NA, is able to achieve a FOV of 3.3 mm × 3.0 mm × 1.0 mm (XYZ).

In Section 2.2 I demonstrate its applicability to optical neuroimaging of juvenile Zebrafish. Showing data of *Danionella translucida*, I then motivate why a further optimized OPM with an intermediate NA promises higher quality data.

Since the diffractive re-imaging step of DOPM only works for low NA due to mechanical constraints, I therefore developed image transfer oblique plane microscopy (IOPM), which I present in Section 2.3. IOPM operates at intermediate NA, such as 0.5 NA in the case of this work. My second system implements the re-imaging step by employing a fiber optical face plate to guide the light onto a straight plane and achieves a FOV of 1.5 mm $\times$ 2.3 mm $\times$ 1 mm. In Section 2.4. I show that this IOPM is ideally suited for optical neuroimaging of DT by recording neural activity from the entire brain of *Danionella translucida* at the rate of 1Hz during auditory stimulation.

2 Results

2.1 Methods Development and Characterization: Diffractive Oblique Plane Microscopy (DOPM)

In order to create an OPM system, that is able to cover large FOVs, I conceived, designed, and build a diffractive oblique plane microscope (DOPM) as shown in Figure 5. At the heart of the DOPM is a new solution to the OPM re-imaging step that operates at low NA. Instead of the conventional OPM re-imaging step (Figure 4c), a blazed reflective grating is inserted co-planar with the intermediate image plane. Excited fluorescence in the object will therefore be imaged onto this grating surface. Here the light is diffracted into a tertiary imaging system and therefore can be captured even at low NA (Figure 5a).

After preliminary experiments that ensured that diffractive re-imaging with a grating would in principle be possible, I selected a commercially available grating with period $d = 555$ nm (GR, $26.7°$ blaze, $1800/$mm, Richardson 33025FL01- 290R) based on the grating equation $d = n \cdot \lambda \cdot \sin(\alpha - \beta)$, where β is the angle of the diffracted light , λ is the wavelength, d is the period of the blazed grating, α is the incidence angle and m is the diffraction order. This choice resulted in three allowed diffraction orders $m = 2, 1, 0$ predicted at $\beta = 60.4, 2.8$ and $75.4°$, of which the $m = 1$ diffraction order was measured to carry 43% (at $\lambda = 532$ nm) of the incident light and therefore indeed allowed for a diffractive re-imaging.

I then constructed an OPM around this re-imaging configuration, which I optimized for both a large FOV and to satisfy mechanical constraints needed to insert the grating (Figure 5b). I selected a 4x objective with a NA of 0.28 as the primary, secondary and tertiary imaging lens, since it has a long working distance and one of the largest space-bandwidth products (FOV x NA) among commercially available lenses. The DOPM design in its final form therefore consists of two identical imaging systems, consisting of the objective and a suitable scan lens, placed back to back, that create an intermediate image (IM) of the oblique plane at intermediate image plane (IIM). To excite the oblique plane in the specimen a scanned Gaussian beam is coupled into the optical system via a dichroic mirror so that it is eventually imaged off-axis at the back focal aperture of the primary imaging objective. Furthermore a large-aperture scanning mirror is brought maximally close to the back-focal aperture of the primary objective, which in our case specifically is located 16.2mm outside of the objective. With this arrangement, both, excitation laser and emission light, are scanned and de-scanned via the mirror, which allows for dynamically changing the image plane in the specimen. A tertiary imaging system consisting of a microscope and tube lens then images the surface of the grating, whose surface coincides with intermediate image of the oblique plane, onto the camera (Hamamatsu ORCA flash). The camera sensor contained 2048×2048 pixels with a pixel pitch of 6.5 µm. Using a region of 2048×616 pixels yielded an effective FOV of 3328 µm (X) $\times$ 1001 µm (Z) at the grating plane. This matched the confocal parameter and approximate axial imaging range of the Gaussian excitation beam. Furthermore, it allowed us to increase the permissible frame rate to 333 Hz. For volumetric imaging, this image plane could be scanned by 1500 µm in y with

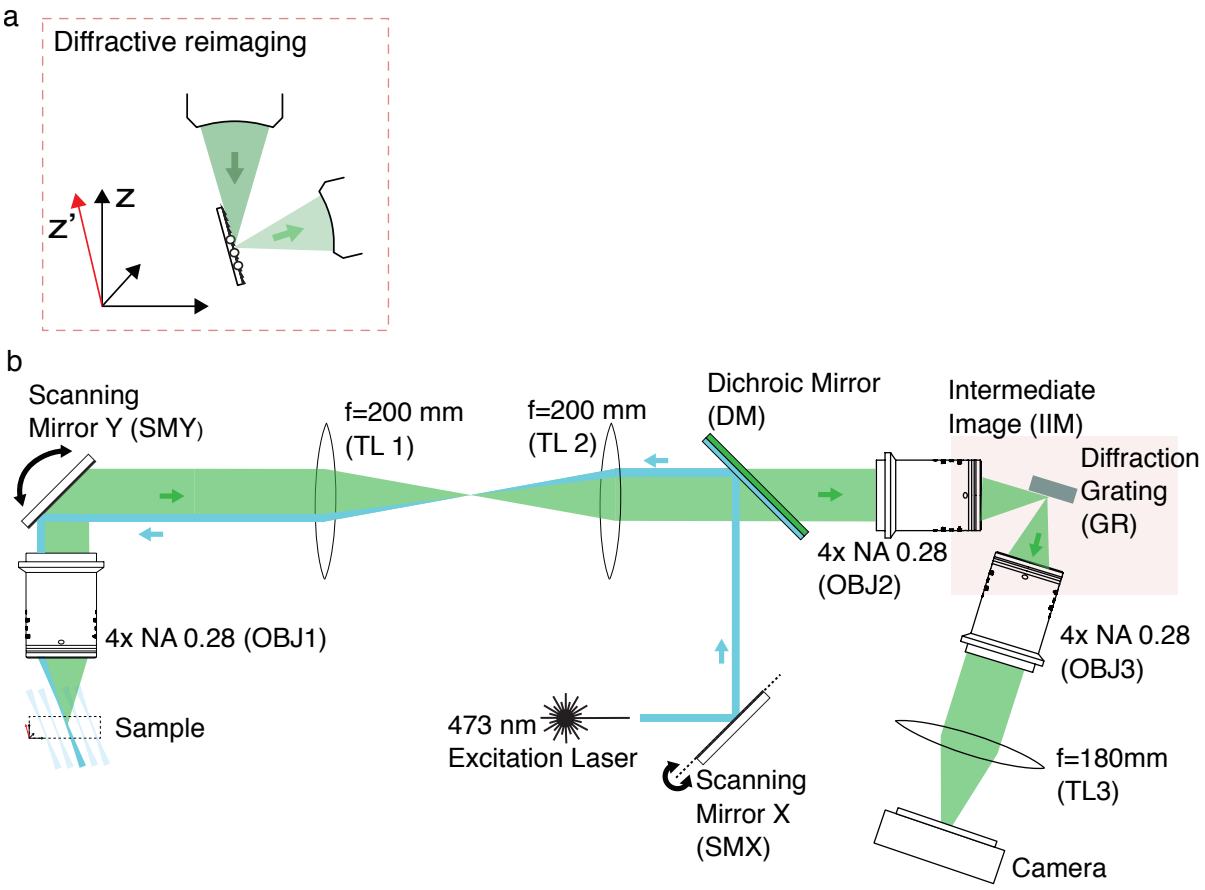

Figure 5: Diffractive Oblique Plane Microscopy – *(a) The Diffractive Re-imaging Step – the surface of a diffraction grating coincides with the intermediate image of the oblique plane. Because the light is diffracted in an almost perpendicular direction it can be captured by the next imaging system, (b) The Setup - a laser focus at the galvanometric scanning mirror (SMX) is imaged onto a de-centered spot at the backfocal aperture of the imaging objective OBJ1 by the 4f system consisting of the two tube lenses TL1 and TL2. This leads to an oblique incidence at the sample. Scanning the mirror SMX excites fluorescence in an oblique plane. The emitted fluorescence from the oblique plane is imaged onto a blazed diffraction grating (GR) at the intermediate image plane (IIM) with unit magnification by means of two identical imaging systems (OBJ1 TL1, OBJ2 TL2). The surface of the diffraction grating (GR) is imaged by a third imaging system (OBJ3, TL3) placed perpendicular to the grating surface. The third imaging system collects the diffracted fluorescence at the IIM and images it onto the camera. A volume is imaged by scanning and de-scanning the imaging plane in the sample by scanning the galvanometric scanning mirror SMY. Adapted from [66]*

help of the galvanometric scanning mirror (SMY), resulting in an accessible imaging volume of 3.3 mm $\times$ 3.0 mm $\times$ 1.0 mm ($X \times Y \times Z$).

In order to verify the instrument's functionality and measure its performance an artificial volumetric sample of fluorescent beads (diameter 1 µm) was imaged with the DOPM as described in [66]. This verified a constant resolution of $2.6 \times 3.1 \times 37.4$ µm^3 over a FOV of 3.3 mm $\times$ 3.0 mm $\times$ 1.0 mm resulting in 3.5×10^7 resolvable image points (Figure 6)

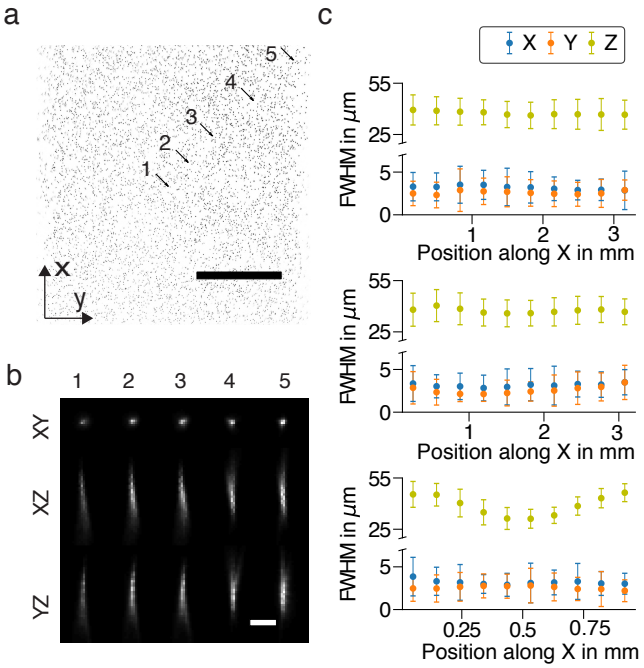

Figure 6: Resolution of Diffractive Oblique Plane Microscopy - *(a) Beads in full FOV, maximum intensity projection of bead volume after shear transformation (ST), scale bar 1000 µm. (b) Example beads, maximum intensity projections of five 1 µm sized beads along x, y, and z after ST; the location in the total FOV is indicated by the arrows in (a), scale bar 20 µm. (c) Resolution across the FOV; each plot shows the dependency of the resolution (mean ± SD) along x, y, and z on bead position along x, y, and z (top to bottom). Taken from [66]*

2.2 Methods Application: Imaging of *Danio Rerio* and *Danionella translucida*

In accordance with my design goals, the FOV of the DOPM was large enough to accommodate larval and juvenile zebrafish ([66] and Figure 7a). To demonstrate that the microscope is indeed useful for neuroimaging, I imaged neural activity in larval and juvenile Zebrafish by recording a subset of the FOV containing the specimen. I was able to image neural activity throughout the whole nervous system of Zebrafish larva throughout the microscope's FOV [66]. Furthermore I was able to image the whole brain of a juvenile Zebrafish and to extract neural activity of around 1000 regions of interest all over the brain at the speed of 1 Hz (Figure 7a-c). In addition to larval and juvenile Zebrafish, I utilized DOPM to image the whole brain of *Danionella translucida*. Although the whole brain of DT could be accommodated within the FOV of the microscope (Figure 7d) preliminary neuroimaging experiment suggested that the recording quality could benefit from a better optical sectioning capability and an increased resolution. Because of its larger size the present aim was not to image the entire animal, but to record brain of *Danionella translucida* only. Given this aim, the DOPM microscope was indeed not perfectly optimized since the FOV was still larger than what would be needed in order to achieve a coverage of the whole brain of *Danionella translucida*. I therefore designed a system that was better optimized for whole-brain imaging of *Danionella translucida* in terms of both resolution and FOV.

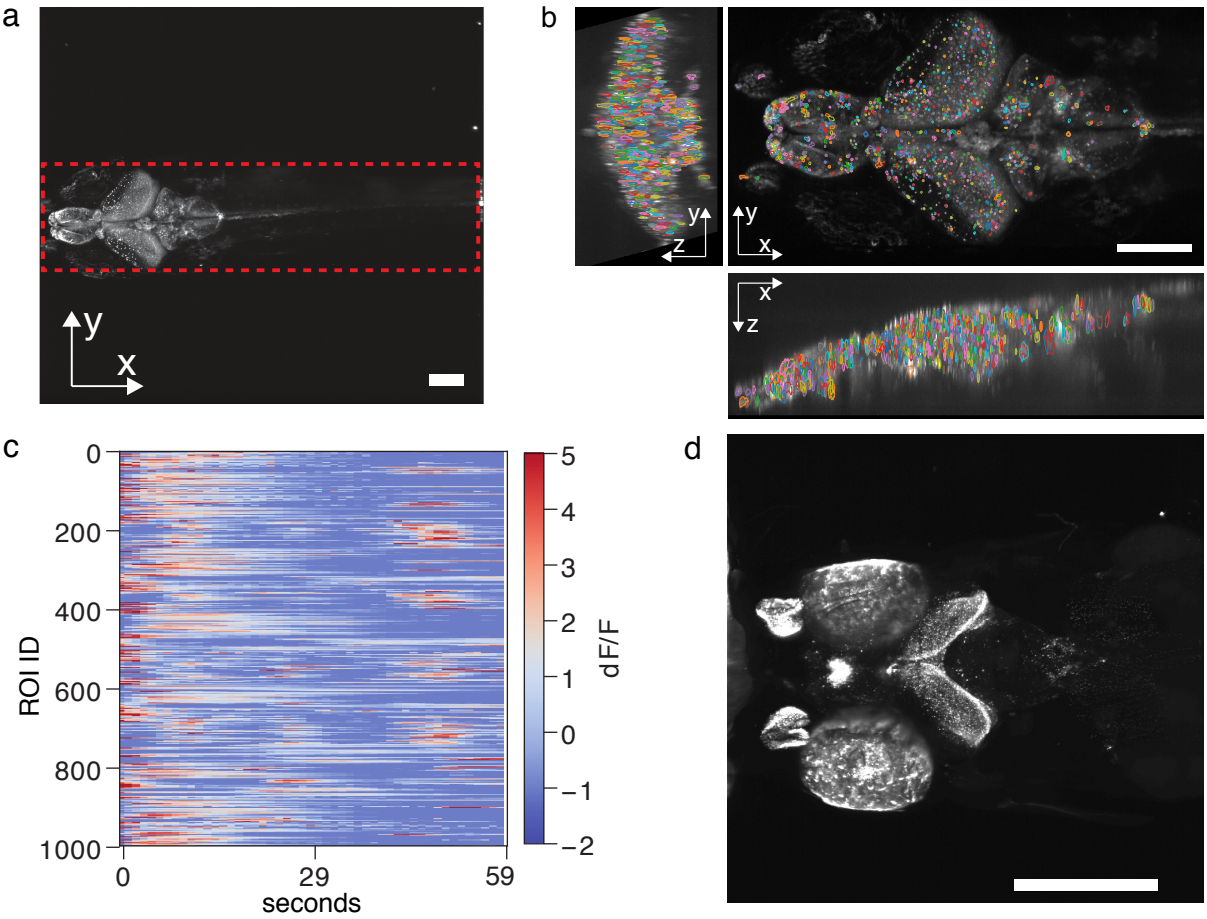

Figure 7: Measurement of neuronal activity over a large field of view (FOV) - *(a) maximum intensity projection of a juvenile zebrafish (Huc: GCaMP6s) in the accessible microscope FOV. The dashed red box represents the region, which was recorded in the time lapse experiments.. (b) MIP of the brain with overlayed contours of the regions of interest along all three dimensions of the volume]. (c) Extracted temporal dF/F traces of the regions of interest shown in (b), (d) a maximum intensity projection of the brain of an adult male DT within the accessible FOV of DOPM (huc:h2b-gcamp6s x tyr); scale bar in (a), (b) 250 µm, in (d) 1000 µm. Source: (a),(b),(c) taken from [66], (d) created by Maximilian Hoffmann.*

2.3 Unpublished Results: Image Transfer Oblique Plane Microscopy

Increasing the resolution and optical sectioning capability of the microscope can be achieved by increasing the NA of the system. Here I determined that using a 10x 0.5 NA objective (Nikon CFI Plan Apo 10XC Glyc) as the primary imaging lens would significantly increase the resolution and optical sectioning of the system, due to the increased angle between emission and excitation light. At the same time the microscope would maintain a FOV big enough to image the entire brain of DT.

However, since the angle of the imaging plane of this new objective is significantly higher, the diffractive re-imaging step introduced in the previous section can no longer be implemented. This is due the mechanical constraints, which do not permit the reflective geometry dictated by the diffraction grating (Figure 8).

I therefore developed a new re-imaging step for the 0.5 NA version of the oblique plane microscope that uses a fiber-optic faceplate. Fiber-optic faceplates consist of an array of closely packed optical fibres and therefoe can be used to transfer an image from one side to the other. We reasoned that, if cut at an approppriate angle, it could therefore be used to transfer the oblique plane onto a straight plane. Here the fiberoptic faceplate had a cut angle of 55 degree, a pitch of 2.5 µm. It was placed at the intermediate image plane, where light is therefore coupled into fibers. The light is then guided to the planar side of the faceplate, where it is emitted at a perpendicular angle and can be imaged by an imaging system.

Around this re-imaging step I designed a new OPM as depicted in Figure 7b. This system is structurally similar to our DOPM system, but deviates in a few points: Because the back-focal aperture (BFP) of this objective is inaccessible, two imaging systems formed by four identical lenses in a 8f-configuration are inserted. These lenses are needed to relay the BFP onto the scanning mirror and then onto the BFP of the second imaging objective (10x 0.45 NA , Nikon CFI Plan Apo Lambda). At this very same point the excitation laser beam is coupled into the system via a small pick-off mirror to circumvent the use of an dichroic mirror and the accompanying induced aberrations. Similar to the DOPM, the secondary objective of the IOPM again forms an intermediate image of the excited oblique plane at the intermediate image plane. At this plane the angled fiber-optic faceplate is placed in order to transfer the oblique onto a parallel plane as described above.

After the light has traversed the faceplate it is then imaged onto the camera (XIMEA CB262MG-GP-X8G3) by the tertiary imaging system consisting of a 10x 0.45 NA (Nikon CFI Plan Apo Lambda 10X) objective and 4x 0.28 NA objective (Olympus XLFLUOR 4x) used as a tube lens. In order to match the confocal parameter of the laser beam, as well as to ensure a frame rate of 333 fps, only a subarray formed by 600 px x 1900 px of the camera sensor was read out. This enabled me to image a FOV of 1.5 mm x 2.3 mm x 1 mm. I then benchmarked the system's performance across the FOV and found a resolution of 1.78 +/- 1.04 µm x 1.38 +/- 0.94 µm x 13.99 +/- 6.02 µm (XYZ). This two-fold improvement in axial resolution due to the higher NA also implied a higher potential for obtaining useful neural data from the whole brain of DT.

2.4 Unpublished results: Mapping Of Auditory Areas of *Danionella translucida* (DT) with IOPM

A fascinating aspect of DT behavior is their acoustic communication by means of sounds that male DT generate. These sounds consist of trains of pulses at 60 or 120 Hz that can last up to minutes [64]. Although the exact role of these acoustic signals in their behavior and ecology are currently not known, the existence of these signals nevertheless immediately poses questions about the neural signature of conspecific acoustic signals and communication.

As a first elementary step towards answering these and more general questions about the auditory system of DT, we attempted to map the auditory areas in the brain by presenting pure tones and artificial replicas of natural vocalisations of male DT while recording neural activity

throughout the whole brain with IOPM (Figure 8). By imaging the 333 oblique planes with an inter-plane separation of 3 µm we were able to record a volume of 0.830 mm x 2.3 mm x 0.71 mm at a volume rate of 1 Hz. This imaging volume contained the entire brain of an adult male DT expressing GCaMP6s in the nucleus of a larger fraction of its neurons (huc:h2b-gcamp6s x tyr -/-). This data allowed us to monitor neural activity throughout the whole brain of DT at a rate of 1Hz during acoustic stimulation. Furthermore throughout the major part of the brain, in which image quality was not compromised by tissue scattering, we could extract neural activity associated with single cell nuclei (Figure 9).

Using a regression analysis we identified the ROIs that were active during the presentation of auditory stimuli (Figure 10a). Areas with auditory-evoked activity were situated throughout the whole brain and we compared these regions with auditory areas described in other fish species that were previously mapped out in histological and functional studies [67]. In the hindbrain we identified regions that likely correspond to the dorso-octavolateral nucleus (DON) and anterior-octavolateral nucleus (AON), which receive input from the primary auditory afferents and project to secondary octaval population (SO) (Figure 10b,c). In the midbrain we identified the Torus Semiscircularis (TSc), the homologue of the mammalian inferior colliculus [68] and central posterior thalamic nucleus (CP). We also observed responses in additional regions, that are considered upstream of the TSc such as in the ventral diencephalon and telencephalon. Although auditory projection and responses that coarsely correspond to these areas have been described in other fish [67], whether these areas really correspond to previously identified areas is currently hard to determine.

In addition to the identification of the auditory areas of DT's brain we also asked, whether we could find functional differences within these areas. Since our stimulus contained pure tones as well as artificial DT vocalisation we asked whether there might be neurons that respond differently to these stimuli, since neurons that are tuned to specific features of typal vocalization have been described in other vocal fish [69]. These previous studies identified these neurons primarily in the TSc of the midbrain and therefore suggested that information content of neural responses become more stimulus specific as activity propagates from hindbrain to midbrain regions.

In order to make a preliminary step towards addressing these questions for the auditory system of DT, we located the neurons that were more responsive to tones than burst and vice versa by comparing the magnitude of their regression coefficients (Figure 10). Interestingly we found neurons with a distinct response to pulses and tone throughout the whole brain, including the TSc, but also the hindbrain nuclei DON and AON. This implies the possibility that information about DT vocalizations might be functionally segregated already at an early stage of the auditory pathway of DT (Figure 10).

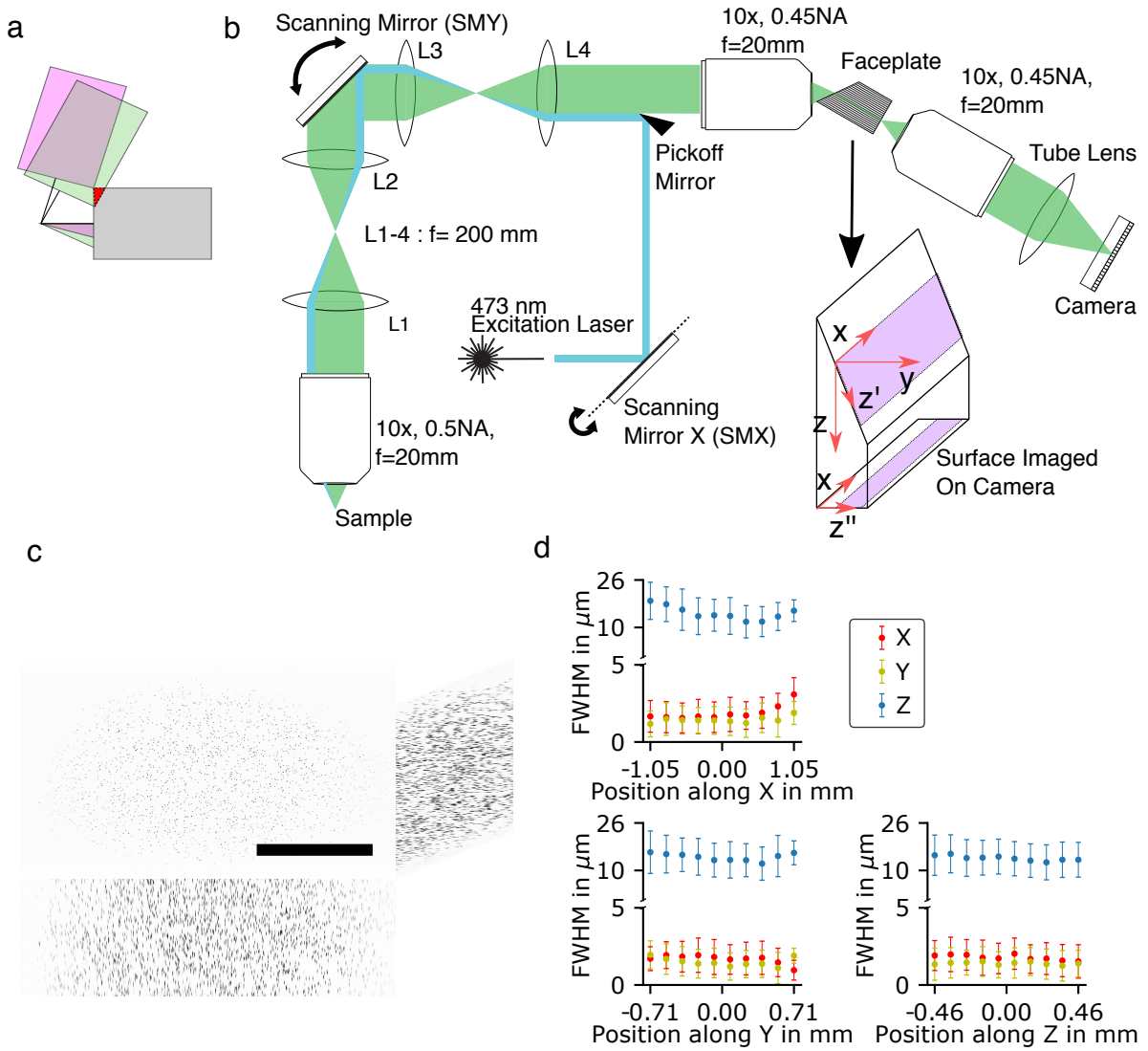

Figure 8: Image Transfer Oblique Plane Microscopy – *(a) Mechanical Constrains of Diffractive Re-Imaging: Higher numerical aperture (NA) of the system leads to mechanical constraints that prohibit diffractive re-imgaging. (Magenta – Low NA, Green – High NA) (b) Setup - The laser focus at the galvanometric scanning mirror (SMX) is imaged onto a de-centered point at a second galvanometric scanning mirror (SMY) via a 4f system (L3,L4). This is then imaged onto the backfocal aperture of the imaging objective OBJ1 by the 4f system consisting of the two tube lenses L1 and L2. This leads to an oblique incidence at the sample. Scanning the mirror SMX excites fluorescence in an oblique plane. The emitted fluorescence from the oblique plane is imaged onto the surface of a slanted fiber-optical faceplate at the intermediate image plane (IIM) with unit magnification by means of three imaging systems (OBJ1 L1, L2 L3, L4 OBJ2). The fluorescence is coupled into one end of the fiber-optical faceplate and guided to the non-slanted surface, which is then imaged onto the camera via a tertiary imaging system (OBJ3 TL5) onto a camera. A volume is imaged by scanning and de-scanning the imaging plane in the sample by scanning the galvanometric scanning mirror SMY. (c) A volume of fluorescent beads (1 µm diameter) imaged by IOPM spanning the whole FOV of 2 mm x 1.4 mm x 1 mm, (d) the resolution throughout the FOV determined by measuring the FWHM of the fluorescent beads in (c). Source: Created by Maximilian Hoffmann*

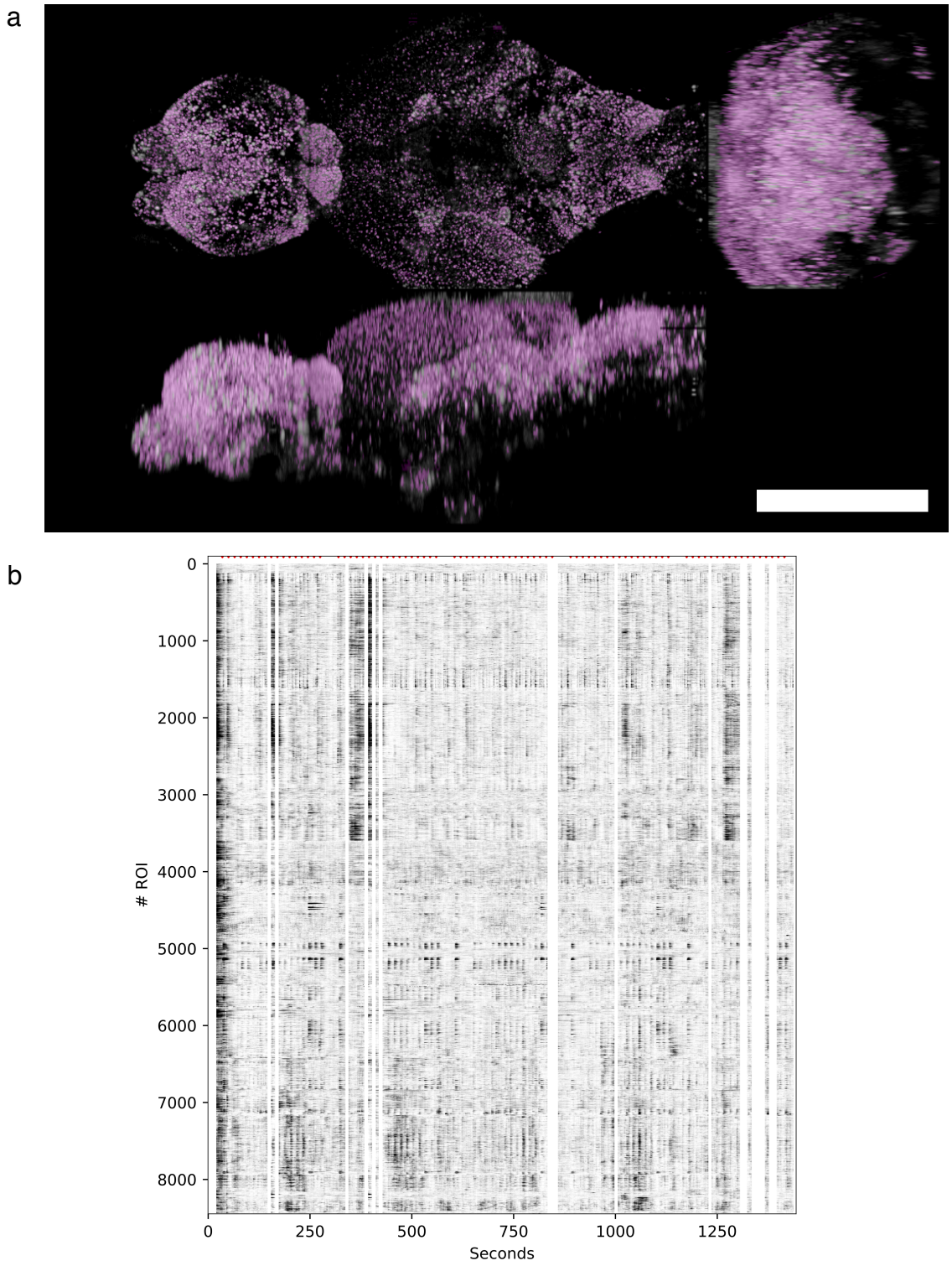

Figure 9: Whole-brain Imaging of Danionella Translucida (DT) during Auditory Stimulation – *(a) Orthogonal maximum intensity projections of a temporally de-noised brain volume of DT (huc:h2b-gcamp6s x tyr -/-) as recorded by the IOPM at 1Hz with overlayed 8447 region of interests (ROIs, magenta), scale bar: 500 µm, (b) dF/F traces of the ROIs in this recording during auditory stimulations. The time of stimulus presentations are indicated by red dots. White areas were removed from display and analysis due to motion artefacts. Source: Created by Maximilian Hoffmann*

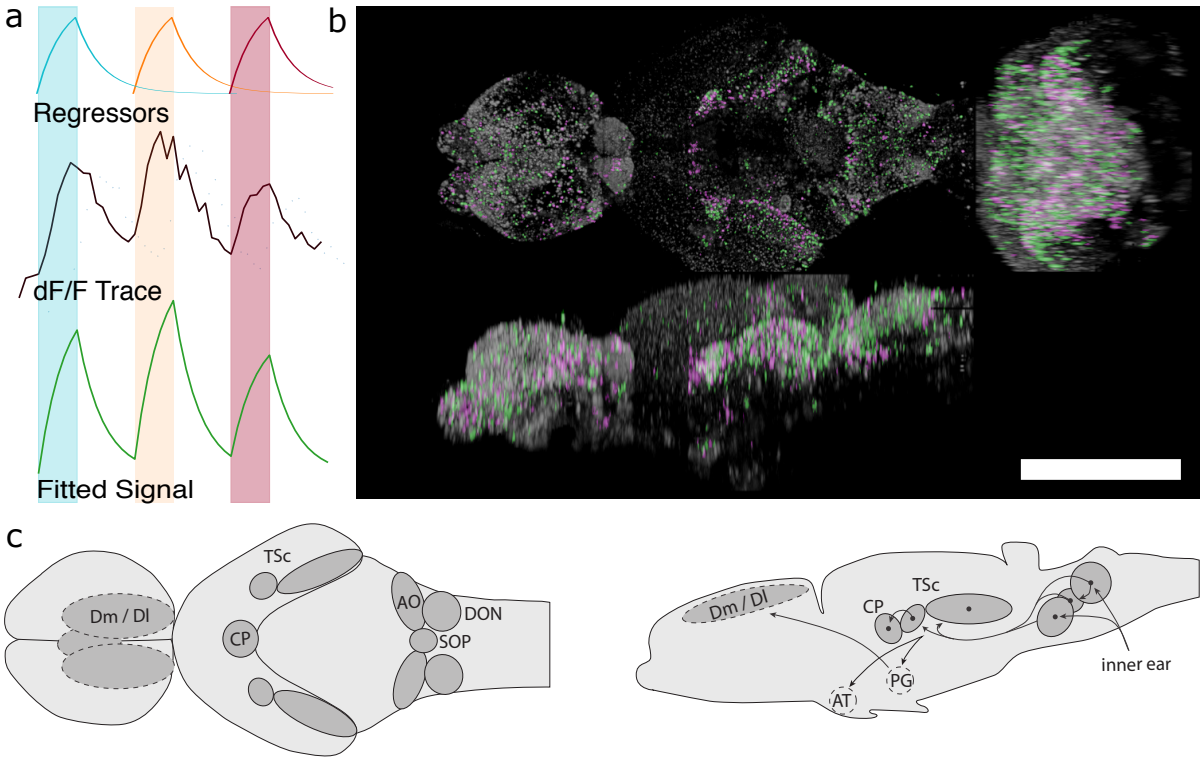

Figure 10: Auditory Areas of Danionella Translucida – *(a) Stimulus response was modelled by exponential kernels to incorporate indicator decay times. The response magnitude was then estimated by non-negative least squares regression (b) Orthogonal projections of maximum intensity projection of a z-cored IOPM volume of DT (huc:h2b-gcamp6s x tyr -/-) with an overlay of 3655 ROIs that respond to auditory stimuli (P>0.6). Green ROIs are more responsive to pure tones (higher regression coefficients), whereas magenta ROIs are more responsive to click sound. (c) the likely position of auditory brain regions forming the ascending auditory pathway of DT (dashed not yet identified) : DON: dorso-octavolateral nucleus, AO: anterior-octavolateral nucleus, SOP: secondary-octaval population, TSc: Torus Semi-circularis , PG: preglomerular nucleus CP: central posterior thalamic nucleus , Dm : medial part of the dorsal telencephalic are, Dl: lateral part of the dorsal telencephalic area, AT: anterior tuberal nucleus of the hypothalamus, scale bar: 500 µm. Source: Created by Maximilian Hoffmann*

3 Discussion and Outlook

The aim of this thesis work was to develop fast imaging tools with a large FOV in order to enable whole brain imaging of the Danionins *Danio rerio* and *Danionella translucida*.

I identified OPM as the most promising technique to achieve this for two main reasons. Firstly, due to its parallel detection scheme, OPM offers the high sampling rates that are needed to record from many neurons. Secondly, it maintains optical sectioning, which is a prerequisite for the imaging of densely labeled tissue at high spatial resolution. However the FOV of conventional OPM is limited, since the common re-imaging step cannot be used at the low NA that would allow FOVs beyond ~ 1 mm.

In order to overcome this limit I developed two novel re-imaging solutions that are compatible with low and intermediate NAs. I conceived and developed two microscopes, DOPM and IOPM, which allowed to extend the FOV of OPM to up to 3mm. Finally, I demonstrated that these techniques are indeed suitable for whole-brain optical neuroimaging of larval and juvenile zebrafish as well as *Danionella translucida*.

In the case of diffractive oblique plane microscopy (DOPM) [66] introduced in section 2.1 a diffraction grating is inserted to re-direct the light at the oblique imaging plane towards a tertiary imaging plane. Using an imaging objective with a low NA of 0.28 my setup trades of NA for FOV and is therefore able to achieve a final FOV of 3.3 mm × 3.0 mm × 1.0 mm, which is one order of magnitude larger than the previous OPMs [44]. At the same time it maintains a resolution of 2.6 × 3.1 × 37.4 μm^3.

Since the reflective geometry of DOPM is increasingly hard to implement for intermediate NAs because of mechanical constraints, I developed image transfer oblique plane microscopy (IOPM) featuring a novel re-imaging step presented in section 2.3. Here the grating is exchanged for a fiber optic faceplate, which permits a transmissive geometry and therefore works well for intermediate numerical apertures. As expected the higher NA of 0.5 led to a significant increase in axial resolution (two-fold) while maintaining a relatively large FOV of 2 mm x 1.4 mm x 1 mm.

Together DOPM and IOPM make it possible to build OPMs at low and intermediate NA's and hereby extend the family of OPM microscopes to FOVs of up to 3mm, which approach FOVs achieved by two-photon microscopes.

DOPM and IOPM were primarily developed to record neural data in a way that facilitates new neuroscientific research of Danionins. I therefore performed neuroimaging expermients that demonstrate their applicability. DOPM allows to image and record neural activity throughout the entire nervous systems of larval and juvenile zebrafish. IOPM is able to optically record neural activity throughout the whole brain of DT at 1 Hz, where in regions that were unaffected by light scattering we could attribute this activity to single cells. As shown in section 2.4 IOPM can be used to create high resolution whole brain activity maps of auditory regions in the DT brain. This allows us to recover large parts of the auditory pathway of cyprinids within in one experimental session of only 15 min.

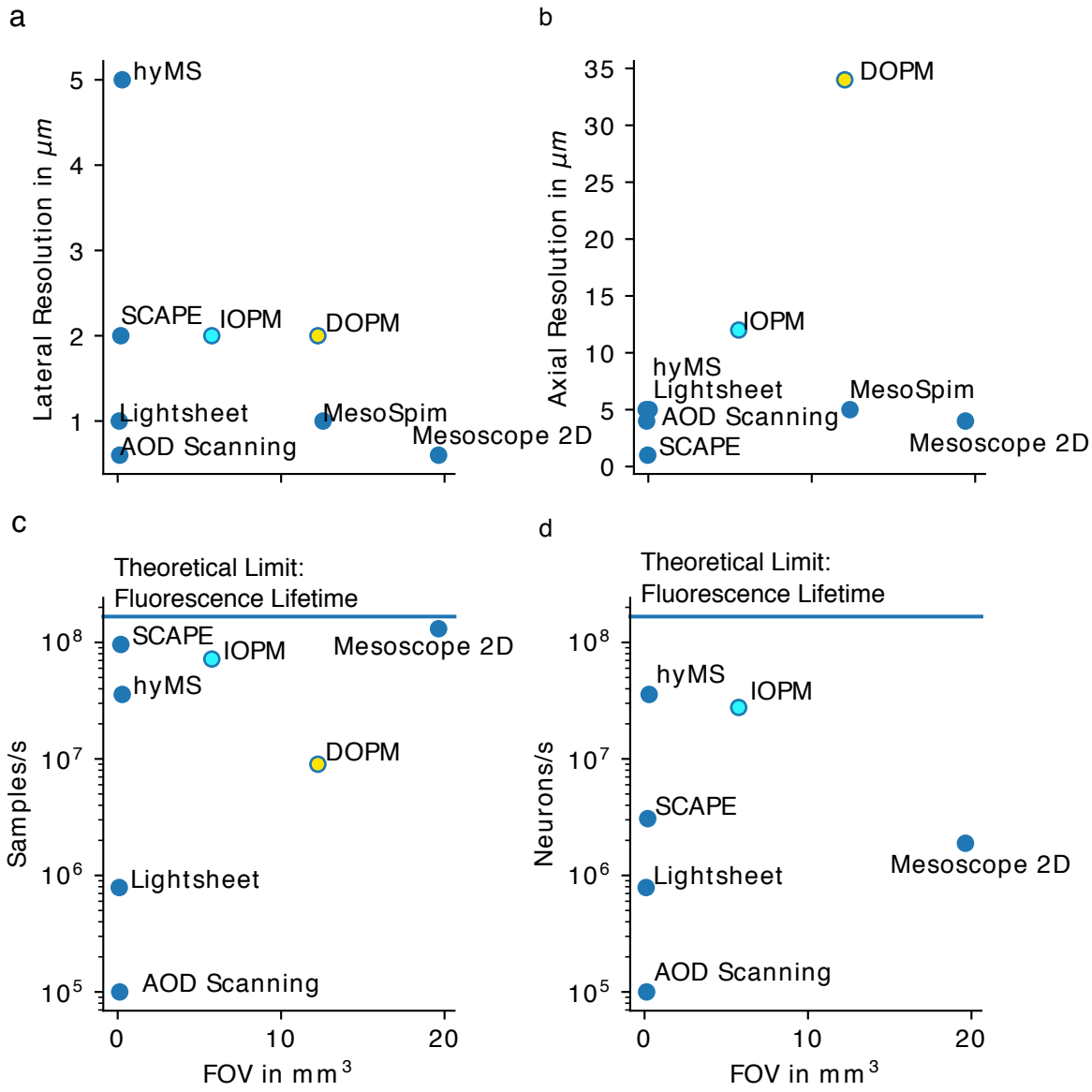

Figure 11: Different Performance Metrics of Neuroimaging Microscopes - *hyMS [70]: a specialized two-photon point scanning microscope that scans a neuron-sized spot through the specimen, and therefore images one neuron per timepoint, SCAPE [44, 71]: a well-known and performant conventional OPM technique, Lightsheet [42]: LSM microscopy as used for whole-brain imaging of larval Zebrafish, Mesoscope [36, 72]: a version of a two-photon pointscanning microscope with a very large FOV, AOD scanning [73, 74]: A microscope that employs fast two-photon pointscanning with help of acousto-optical deflectors (AOD), and IOPM, DOPM as presented in this thesis. Panel (a) and (b) - optical resolution achieved, panel (c) - temporal throughput measured in samples per seconds, (d) - estimated number of neurons that could be recorded per second. (DOPM is omitted in (d) because single cell resolution is disputable.) Source: Created by Maximilian Hoffmann*

Comparison to Other Techniques

With the qualitative comparisons of microscopy techniques from Section 1.3 in mind we can now ask how unique these capabilities of DOPM and IOPM are in comparison to other techniques

and speculate about future developments. Figure 11 compares some performance measures of recently published microscopes with IOPM and DOPM.

These microscopes include two-photon point scanning microscopes such as the hyMS [70], the Mesoscope [36] and the fast random access microscopes based on scanning by acousto-optical deflectors [73, 74], but also a conventional lightsheet microscope as used in [42] and a conventional OPM technique called SCAPE [44]. As expected point-scanning methods outperform the OPM techniques because of their diffraction-limited performance. An exception is hyMS, the resolution of which is intentionally reduced to 5 µm to match a single neuronal soma (Figure 11a,b).

The main objective of this thesis was to at the same time extend the FOV and to retain the high throughput of OPM techniques. Indeed the FOV of IOPM and DOPM are approximately ten times larger than the one achieved by previous techniques such as SCAPE (Figure 11c). This however was only possible by trading-off NA and resolution, which in IOPM and DOPM is therefore reduced in comparison to SCAPE or the light sheet microscope.

Since our technique is aimed at neuroimaging, temporal throughput is equally important. Here an important comparison is the theoretical upper limit to the throughput of point scanning techniques defined as the number of distinct image points that can be recorded per second. For point-scanning methods that sample one point at a time this throughput is capped by the fluorescence lifetime, because faster measurements would lead to signal mixing between consecutive image points. Figure 11c shows that this limit is currently already approached by highly optimized point-scanning techniques like hyMS or the Mesoscope.

OPM with its parallel detection scheme is not subject to this limit. Therefore techniques like SCAPE, IOPM and DOPM routinely achieve rates that are close to this limit and are expected to surpass the limit as more efficient and faster cameras become available. Figure 11c, however, also shows that IOPM and DOPM, the techniques developed here, indeed occupy a unique position by combining this high temporal throughput achieved through parallel detection with a large FOV.

Finally, an important metric for neuroscientific applications is the number of neurons a microscope is able to record from in one second (Figure 11d). Since a neuronal soma in Danionins is $\sim 5 \times 5 \times 5$ µm large we can assess how many of these somata fit into the FOV and could be recorded from during one second given the speed of the microscope. In this comparison we omitted DOPM, because its axial resolution is much larger than needed for true single cell resolution in densely labeled samples.

Again the graph contains a theoretical limit, at which a point scanning microscope would operate at the speed of one neuron per fluorescence lifetime period. Among point-scanning microscopes only hyMS approaches this limit by employing a special high power laser and temporal multiplexing in order to excite one neuron with one laser pulse. Other techniques like the Mesoscope record multiple samples for every neuron and therefore are easily outperformed by microscopes employing parallel detection like the lightsheet microscope or the OPM techniques.

The sampling rate of IOPM is comparable to that of other OPM techniques like SCAPE (Fig-

ure 11c). However due to its favourable choice of trade-off between resolution and FOV it is potentially able to record from as many neurons as the fastest point scanning microscope (Figure 11d). At the same time it maintains a FOV that is 30x larger than previous OPM techniques used for neuroimaging.

Possible Future Improvements

Despite their unique capabilities, DOPM and IOPM both remain complementary to other microscopy techniques, but future developments and optical research will likely increase the range of their applicability. The speed of DOPM and IOPM will be able to exceed the theoretical speed of point scanning microscopes as faster and more sensitive cameras become available. These techniques would still remain vulnerable to scattering because of their one-photon excitation. However this could partially mitigated by structured illumination [75] and confocal-slit detection [76] combined with potential non-linear illumination.

Aiming for a large FOV, DOPM and IOPM both have a lower axial resolution than previous version of OPM [52, 46] due to the reduced NA. Future custom optics might be able to increase the NA of our systems, while maintaining their current FOV. Although the re-imaging steps were developed for low and intermediate NA, even for higher NAs, our re-imaging step would be more light efficient than conventional OPM [66]. It would therefore be preferable to implement our OPM re-imaging step even at slightly higher NAs, if the system is to be optimized for light efficiency. Finally, without an additional increase of the NA of the system, the resolution of both OPM systems could be improved via a multi-view deconvolution approach to OPM [77, 78]. Here two OPM volumes taken from different direction are computationally combined to increase sectioning capability and resolution.

New Possibilities For Neuroscience

Already in their present form, both systems will enable novel interesting neuroscientific research. DOPM with its increased FOV that can accommodate multiple larval Zebrafish, will be an attractive option for future studies that may involve freely moving larval zebrafish [60] or social interactions of several Zebrafish larvae [79]. Additionally it could be of interest for investigating the motor system, since the spinal cord and brain can be imaged at the same time, even in juvenile zebrafish [80].

As shown in section 2.4, IOPM is well suited to image neural population activity throughout the whole-brain and of whole sensory pathways of DT at 1Hz. It will therefore be a valuable tool to further functionally characterize the auditory brain regions and to investigate the neural basis of the sensory processing of the acoustic communication of DT.

Of course the current imaging technique is not limited to investigations of the auditory system, but could be used to investigate other sensory modalities and cognitive functions like memory or learning. Although many neuroscientific questions might be investigated in a sequential manor by tiling the field of view with a point-scanning microscope the microscopes presented here have the advantage of facilitating these experiments due to the high throughput. This might be

especially important in cases where it is unknown where plastic or dynamic changes in the brain might be occurring. This might the case for studies that involve learning of an unknown task or brain regions that are not as well characterized such as the fish pallium.

Beyond that the quasi–simultaneously recording of the whole-brain allows to correlate activity across distant brain regions and will allow to measure how global brain wide activity is organized. It therefore opens the possibility of exciting research into phenomena involving global brain states such as epileptic seizures [81] or anesthesia [45] and the instantaneous correlation of behavioural variability with brain-wide neural activity [82].

Finally, both microscopes have been developed for neuroimaging of Danionins, but their usage of course is not limited to that. Both microscopes might therefore for example be useful in rodent neuroscience. Although their penetration depth would necessarily be quite low due to scattering they could still be an interesting option for imaging layer 1 of cortex including sparsely labeled apical dendrites of pyramidal cells over a large FOV.

Outlook

The contribution of this thesis work to current scientific efforts is therefore two-fold: On the one hand it improved oblique plane microscopy and extended it towards a larger FOV. This improvement is compatible with other concurrent research about OPM [78, 83, 84] and will therefore likely lead to further new developments in the field of microscopy. On the other hand it also created microscopes with unique capabilities that are of immediate use in neuroscientific research of Danionins and beyond. In particular the combination of the OPM techniques developed here with the advantages of the transparent model organism *Danionelle translucida* allows to record neural population activity from the whole brain of an adult vertebrate at 1 Hz. This expanded capability of optical neural population imaging will hopefully lead to new insights into the properties and function of the nervous system at a systemic level.

A Experimental Procedures

A.1 DOPM Setup Details

A detailed description of the DOPM setup can be found in [66].

A.2 IOPM Setup Details

The specimen is re-imaged by a series of three imaging systems (IM1: 10x 0.5 NA objective CFI Plan Apochromat 10XC Glyc + f=200mm, TTL200MP, Thorlabs, IM2: 2x f=200mm, TTL200MP, Thorlabs , IM3: f=200mm, TTL200MP and 10x 0.45 NA Nikon CFI Plan Apo Lambda 10X M). Into the image plane a face plate (FP, Schott 24AS 2.5) , with a slanted surface of 35 degrees (the angle that is formed by the oblique plane and the backsurface) is inserted. The light intensity on the surface of the FP is coupled into the waveguides and imaged by a tertiary imaging system (10x 0.45 NA, Nikon CFI Plan Apo Lambda 10X M and Olympus 4x 0.28 NA XLFLUOR) onto a camera (CB120MG-CM-X8G3, Ximea) The excitation laser (Laser Cobolt 06-MLD 488nm 30 mW , $\omega_0 = 12$µm in the specimen) is directed onto a galvanometric scanning mirror (6 mm, 8315 K, CambridgeTechnology, SMX) and is then deflected off-center into the imaging path by a knife edge mirror, that is placed as close as possible to the BFP of the last objective. The emission as well as the excitation light is de-scanned by (25 mm beam diameter, 6240H,Cambridge Technology, SMY)

A.3 Microscope Control Software and Pipeline

The DOPM was controlled via a custom image acquisition software written in Matlab and C++ that controlled the camera and the data acquisition card (NI-USB6363, National Instruments). The IOPM was controlled via a custom image acquisition software written in Python and C++, which controlled the camera and the data acquisition card (NI-USB6363, National Instruments). Before each acquisition a background frame was recorded (mean of 100 images at selected exposure time). This background was then subtracted from each imaged plane. Since the OPM acquires data in a sheared coordinate system (Figure 12) prior to all data analysis the data was transformed to the rectilinear lab coordinate system from its native sheared geometry. In the case of DOPM this was done via the 3d affine transformation A= [[1 0 0 0],[0 1 –tan(θ) 0],[0 0 cos(θ) 0],[0 0 0 1]] (homogeneous coordinates, scale and shear), where θ is the grating angle with respect to the optical axis. This was done either by imwarp (Matlab, Mathworks Inc. , linear interpolation) or warpAffine (opencv 3, linear interpolation). In the case of IOPM de-shearing was done via a simple pixel shift that corresponded to the shearing angle in the system. (Figure 12)

In case of the IOPM the data frequently contained movement artefacts, which were corrected by a custom image registration code using pyANTS and scikit-image. The registration was done using a piece-wise rigid motion correction (Figure 12b). A single frame in our recording was se-

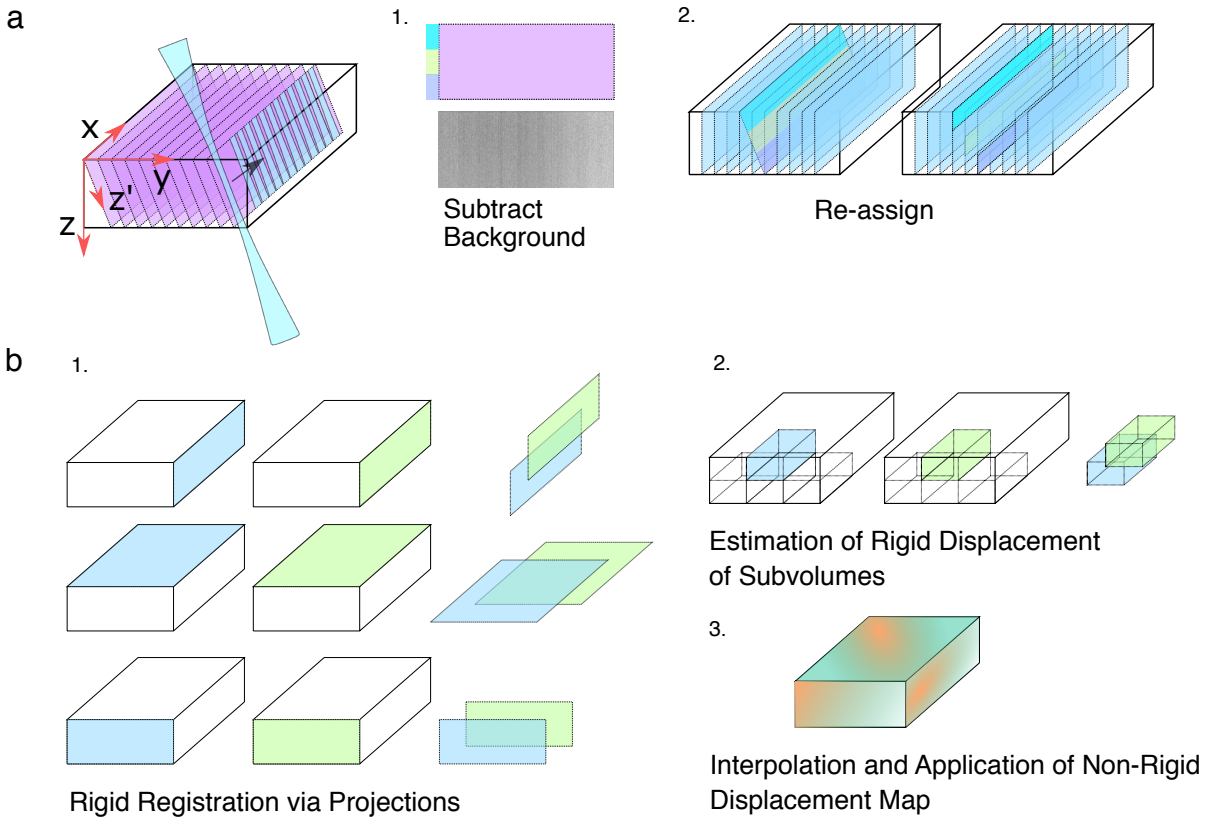

Figure 12: Image Processing Pipeline - *a) With an OPM images are acquired in a sheared geometry. In order to work in a normal Cartesian frame of reference the volume is de-sheared after background subtraction. b) Motion occurring during timelapse imaging of the IOPM is corrected by a rigid motion correction via cross-correlations of maximum intensity projection. As a second step a rigid displacement is estimated for sub-volumes via cross-correlation. This coarse displacement is then interpolated to a non-rigid displacement map and applied to the volume. Source: Created by Maximilian Hoffmann*

lected as a reference volume. For every volume in our recording a rigid 3D displacement was determined by estimating the shift via the phase correlation of all 3 possible 2D maximum intensity projections. After correcting for global displacement, non-rigid displacement was then carried out by locally estimating the 3D displacement on chunks of the data (128 px $\times$ 128 px $\times$ 128 px). The resulting coarse displacement field was interpolated to yield a smooth displacement map at the single pixel level, which was then applied to the volume.

A.4 Resolution Measurements With Volumetric Beads

Fluorescent beads (diameter 1 µm) were dispersed in a poly-acrylamide gel between a coverslide and a coverslip held apart by a silicon spacer. A stack of the whole accessible image volume at an isotropic voxel size of 1.625 µm was taken. The stack was then transformed as described in section A. The stack was thresholded at the 99.99th percentile and all connected

components were segmented out within a ROI of 33×33×303 µm (X×Y×Z) For the quantification of the lateral resolution each ROI was maximum intensity projected along z. The lateral resolution in x and y were determined as the full width at half maximum (FWHM) of the line plot through the maximum of this projection. The axial sectioning capability was determined as the FWHM of the sum of all pixel values along the XY planes of each bead volume. Often two or more beads were axially contained in one ROI, which manifested in a bimodal distribution of the axial sectioning FWHM. This bi-modal distribution was fit by a Gaussian mixture model. The ROIs belonging to the distribution with the higher mean and therefore contained multiple beads were excluded from the analysis.

A.5 Animal Husbandry

DT specimens were kept in commercial zebrafish aquaria (Tecniplast) with the following water parameters: pH 7.3, conductivity 350 μS/cm, temperature 27 °C.

Zebrafish specimens were kept in commercial zebrafish aquaria (Tecniplast) with the following water parameters: pH 7.3, conductivity 745 μS/cm, temperature 27 °C.

Zebrafish larvae were raised at 24 degrees celsius. For the first 24 hours embryos developed in embryo medium [85]. Afterward, larvae were exclusively raised in A2000 solution.

A.6 Animal Experiments

All animal experiments conformed to Berlin state, German federal and European Union animal welfare regulations and were approved by the LAGeSo, the Berlin admission authority for animal experiments:

The license used for Zebrafish experiments was G0171/15 (Issued 26.08.2015).

The license used for experiments with *Danionella translucida* was G0317/16 (Issued 26.04.2017)

A.6.1 Imaging of Juvenile Zebrafish

A juvenile Zebrafish larva (nacre, elavl3:H2B-GCaMP6s) was restrained by embedding it in agarose (2% Low melting point) and placed under the microscope. All images were taken with 3 ms exposure time, a 2 ms lasersweep time and an average laser power of 11mW at the image plane.

A.6.2 Imaging of DT

DT were put into a pre-formed agarose mold, which allowed the gills to move freely, and immobilized with 2% low-melting point agarose. A mouthpiece, made from a glass pipette was inserted into their mouth and the fish were then perfused with filtered system water via a peristaltic pump. The excitation beam had a power of $\approx$5.3 mW after the imaging objective. It was

scanned through one plane in 2ms. This coincided with the 2 ms sensor exposures. Recording and read-out of one plane took 3.1 ms. We could therefore image 332 planes spanning 827.5 µm at 1 Hz volume rate.

A.6.3 Imaging of DT during Auditory Stimulation

Stimulus presentation was controlled by a module of the microscope software and streamed via a second DAQ card (NI-USB6363, National Instruments), which shared a clock signal with the microscope. The signal was delivered to an audio amplifier (Apart Champ Four), whose output was fed into an loudspeaker (VIS2801, Visaton), which was embedded beside the fish. The stimulus presentation began 120 seconds after the recording started, in order to wait for adaptation of the fish to blue light. The stimuli consisted of pure sine tones of 30, 45, 60, 75, 90, 105, 120, 140, 160, 180, 250, 300 and 400 Hz and pulse trains of 60 and 120 Hz. The pulse trains consisted of individual pulses of the form

$$I(t) = 2\pi \cdot 5000\text{Hz} \cdot t \cdot \exp^{-2(\pi \cdot 5000\text{Hz} \cdot t)^2}$$

. At this point the amplitude of the stimuli was arbitrarily chosen to be 1V for the tones and 6V for the pulses (peak-to-peak, measured before the speaker). The stimuli lasted 5 second and were separated by 10 seconds of silence. The block of all stimuli was presented 5 times.

A.7 ROI Segmentation Zebrafish

The extraction of fluorescence traces and spatial footprints from single cells was done by performing the cell segmentation of the CaImAn package[86] on subblocks of the imaging data with greedyROI initialisation. The footprints and traces where then aggregated and only ROIs with a standard deviation above the 70.1th percentile were kept. This threshold was chosen, as it was seen to reject spurious and noisy ROIs by manual inspection. ΔF/F traces were calculated by subtracting and dividing each extracted trace by its temporal mean.

A.8 ROI Segmentation DT

For the purpose of ROI segmentation the 4D data is de-trended by removing the first spatial PCA. Subsequently a contrast enhanced map of the volume is calculated via temporal PCA. The spatial loadings of the first 200 temporal principal components are computed. The map is than created by averaging these component weighted by their explained variance. The resulting volume is therefore equivalent to a denoised z-scored volume. Seed voxels for ROI segmentation are determined by finding the local maxima in this volume. Afterwards it is thresholded above its 90th percentile. The final ROI mask is then computed by thresholding the local correlation map of the temporal PCAs around the seed voxel at P= 0.5.

A.9 Regression Analyis DT

dF/F0 was calculated as F(t)-mean(F(t))/F(t). Regressors where build by convolving stimulus indicator functions with exponential kernels of varying decay times from 0 to 5 s that modelled the underlying calcium and fluorescence decay. The signal of each ROI was regressed onto these regressors using non negative least squares. The regression coefficients of the regression run with the highest R2 value was kept.

B Bibliography

[1] NobelPrize.org. Nobel Media AB 2020, ed. *Camillo Golgi – Facts*. URL: https://www.nobelprize.org/prizes/medicine/1906/golgi/facts/.

[2] R D Hawkins, N Lalevic, G A Clark and E R Kandel. "Classical conditioning of the Aplysia siphon-withdrawal reflex exhibits response specificity." In: *Proceedings of the National Academy of Sciences of the United States of America* 86.19 (Oct. 1989), pp. 7620–7624.

[3] Horace B Barlow. "Possible principles underlying the transformation of sensory messages". In: *Sensory communication* 1 (1961), pp. 217–234.

[4] Eric R Kandel, James H Schwartz, Thomas M Jessell, Department of Biochemistry, Molecular Biophysics Thomas Jessell, Steven Siegelbaum and AJ Hudspeth. *Principles of neural science*. Vol. 4. McGraw-hill New York, 2000.

[5] Peter Dayan and Laurence F Abbott. *Theoretical neuroscience: computational and mathematical modeling of neural systems*. Computational Neuroscience Series, 2001.

[6] Juan A Gallego, Matthew G Perich, Raeed H Chowdhury, Sara A Solla and Lee E Miller. "Long-term stability of cortical population dynamics underlying consistent behavior". In: *Nature neuroscience* 23.2 (2020), pp. 260–270.

[7] Kevin L Briggman, Henry DI Abarbanel and William B Kristan Jr. "From crawling to cognition: analyzing the dynamical interactions among populations of neurons". In: *Current Opinion in Neurobiology* 16.2 (Apr. 2006), pp. 135–144.

[8] Peiran Gao, Eric Trautmann, Byron Yu, Gopal Santhanam, Stephen Ryu, Krishna Shenoy and Surya Ganguli. "A theory of multineuronal dimensionality, dynamics and measurement". In: *bioRxiv* (2017). DOI: 10.1101/214262. URL: https://www.biorxiv.org/content/early/2017/11/05/214262.

[9] William E Allen, Michael Z Chen, Nandini Pichamoorthy, Rebecca H Tien, Marius Pachitariu, Liqun Luo and Karl Deisseroth. "Thirst regulates motivated behavior through modulation of brainwide neural population dynamics". In: *Science* 364.6437 (Apr. 2019).

[10] Carsen Stringer, Marius Pachitariu, Nicholas Steinmetz, Charu Bai Reddy, Matteo Carandini and Kenneth D Harris. "Spontaneous behaviors drive multidimensional, brainwide activity". In: *Science* 364.6437 (Apr. 2019), eaav7893.

[11] Ian H Stevenson and Konrad P Kording. “How advances in neural recording affect data analysis”. In: *Nature Neuroscience* (Jan. 2011), pp. 1–4.

[12] Edgar Douglas Adrian. *The basis of sensation.* WW Norton & Co, 1928.

[13] Birdsey Renshaw, Alexander Forbes and BR Morison. “Activity of isocortex and hippocampus: electrical studies with micro-electrodes”. In: *Journal of neurophysiology* 3.1 (1940), pp. 74–105.

[14] David H Hubel and Torsten N Wiesel. “Receptive fields of single neurones in the cat’s striate cortex”. In: *The Journal of physiology* 148.3 (1959), p. 574.

[15] Guosong Hong and Charles M Lieber. “Novel electrode technologies for neural recordings”. In: *Nature Reviews Neuroscience* 20.6 (2019), pp. 330–345.

[16] James J Jun, Nicholas A Steinmetz, Joshua H Siegle, Daniel J Denman, Marius Bauza, Brian Barbarits, Albert K Lee, Costas A Anastassiou, Alexandru Andrei, Çağatay Aydın, Mladen Barbic, Timothy J Blanche, Vincent Bonin, João Couto, Barundeb Dutta, Sergey L Gratiy, Diego A Gutnisky, Michael Häusser, Bill Karsh, Peter Ledochowitsch, Carolina Mora Lopez, Catalin Mitelut, Silke Musa, Michael Okun, Marius Pachitariu, Jan Putzeys, P Dylan Rich, Cyrille Rossant, Wei-lung Sun, Karel Svoboda, Matteo Carandini, Kenneth D Harris, Christof Koch, John O’Keefe and Timothy D Harris. “Fully integrated silicon probes for high-density recording of neural activity”. In: *Nature* 551.7679 (Nov. 2017), pp. 232–236.

[17] S Ogawa, Lee T M, A S Nayak and P Glynn. “Oxygenation-Sensitive Contrast in Magnetic-Resonance Image of Rodent Brain at High Magnetic-Fields”. In: *Magnetic Resonance in Medicine* 14.1 (Apr. 1990), pp. 68–78.

[18] Adam Marblestone, Bradley Zamft, Yael Maguire, Mikhail Shapiro, Thaddeus Cybulski, Joshua Glaser, Dario Amodei, P Benjamin Stranges, Reza Kalhor, David Dalrymple, Dongjin Seo, Elad Alon, Michel Maharbiz, Jose Carmena, Jan Rabaey, Edward Boyden, George Church and Konrad Kording. “Physical principles for scalable neural recording”. In: *Frontiers in Computational Neuroscience* 7 (2013), p. 137.

[19] RD Allen and GB David. “The Zeiss-Nomarski differential interference equipment for transmitted-light microscopy”. In: *Zeitschrift fur wissenschaftliche Mikroskopie und mikroskopische Technik* 69.4 (1969), pp. 193–221.

[20] Adolf Friedrich Fercher. “Optical coherence tomography”. In: *Journal of biomedical optics* 1.2 (1996), pp. 157–174.

[21] Jerome Mertz. *Introduction to optical microscopy*. Cambridge University Press, 2019.

[22] Bernard Valeur. “Molecular fluorescence”. In: *Digital Encyclopedia of Applied Physics* (2003), pp. 477–531.

[23] Roger Y Tsien. “The green fluorescent protein”. In: *Annual review of biochemistry* 67.1 (1998), pp. 509–544.

[24] Martin Chalfie, Yuan Tu, Ghia Euskirchen, William W Ward and Douglas C Prasher. “Green fluorescent protein as a marker for gene expression”. In: *Science* 263.5148 (1994), pp. 802–805.

[25] Amiram Grinvald, Edmund Lieke, Ron D Frostig, Charles D Gilbert and Torsten N Wiesel. “Functional architecture of cortex revealed by optical imaging of intrinsic signals”. In: *Nature* 324.6095 (Nov. 1986), pp. 361–364.

[26] Kathleen M Carter, John S George and David M Rector. “Simultaneous birefringence and scattered light measurements reveal anatomical features in isolated crustacean nerve”. In: *Journal of Neuroscience Methods* 135.1-2 (May 2004), pp. 9–16.

[27] Grzegorz Grynkiewicz, Martin Poenie and Roger Y Tsien. “A new generation of Ca2+ indicators with greatly improved fluorescence properties.” In: *Journal of biological chemistry* 260.6 (1985), pp. 3440–3450.

[28] MB Cannell, JR Berlin and WJ Lederer. “Intracellular calcium in cardiac myocytes: calcium transients measured using fluorescence imaging”. In: *Soc. Gen. Physiol. Ser.* 42 (1987), pp. 201–214.

[29] Donald M O’Malley, Yen-Hong Kao and Joseph R Fetcho. “Imaging the Functional Organization of Zebrafish Hindbrain Segments during Escape Behaviors”. In: *Neuron* 17.6 (Dec. 1996), pp. 1145–1155.

[30] Werner Göbel and Fritjof Helmchen. “In Vivo Calcium Imaging of Neural Network Function”. In: *Physiology* 22.6 (Dec. 2007), pp. 358–365.

[31] Christine Grienberger and Arthur Konnerth. “Imaging calcium in neurons”. In: *Neuron* 73.5 (2012), pp. 862–885.

[32] Junichi Nakai, Masamichi Ohkura and Keiji Imoto. “A high signal-to-noise Ca 2+ probe composed of a single green fluorescent protein”. In: *Nature biotechnology* 19.2 (2001), pp. 137–141.

[33] Tsai-Wen Chen, Trevor J Wardill, Yi Sun, Stefan R Pulver, Sabine L Renninger, Amy Baohan, Eric R Schreiter, Rex A Kerr, Michael B Orger, Vivek Jayaraman, Loren L Looger, Karel Svoboda and Douglas S Kim. “Ultrasensitive fluorescent proteins for imaging neuronal activity”. In: *Nature* 499.7458 (July 2013), pp. 295–300.

[34] Roarke Horstmeyer, Maximillian Hoffmann, Haowen Ruan, Benjamin Judkewitz and Changhuei Yang. “Imaging Deep in the Brain with Wavefront Engineering”. In: *Handbook of Neurophotonics* (2020), p. 147.

[35] W Denk, J H Strickler and W W Webb. “Two-photon laser scanning fluorescence microscopy”. In: *Science* 248.4951 (Apr. 1990), pp. 73–76.

[36] Nicholas James Sofroniew, Daniel Flickinger, Jonathan King and Karel Svoboda. “A large field of view two-photon mesoscope with subcellular resolution for in vivo imaging.” In: *eLife* 5 (June 2016), p. 413.

[37] Sara Abrahamsson, Jiji Chen, Bassam Hajj, Sjoerd Stallinga, Alexander Y Katsov, Jan Wisniewski, Gaku Mizuguchi, Pierre Soule, Florian Mueller, Claire Dugast Darzacq, Xavier Darzacq, Carl Wu, Cornelia I Bargmann, David A Agard, Maxime Dahan and Mats G L Gustafsson. “Fast multicolor 3D imaging using aberration-corrected multifocus microscopy”. In: *Nature Methods* 10.1 (Dec. 2012), pp. 60–63.

[38] Robert Prevedel, Young-Gyu Yoon, Maximilian Hoffmann, Nikita Pak, Gordon Wetzstein, Saul Kato, Tina Schrödel, Ramesh Raskar, Manuel Zimmer, Edward S Boyden and Alipasha Vaziri. “Simultaneous whole-animal 3D imaging of neuronal activity using light-field microscopy”. In: *Nature Methods* 11.7 (May 2014), pp. 727–730.

[39] Michael Broxton, Logan Grosenick, Samuel Yang, Noy Cohen, Aaron Andalman, Karl Deisseroth and Marc Levoy. “Wave optics theory and 3-D deconvolution for the light field microscope”. In: *Optics Express* 21.21 (2013), pp. 25418–22.

[40] Marc Levoy, Ren Ng, Andrew Adams, Matthew Footer and Mark Horowitz. “Light field microscopy”. In: *Acm Transactions on Graphics* 25.3 (July 2006), pp. 924–934.

[41] Jan Huisken, Jim Swoger, Filippo Del Bene, Joachim Wittbrodt and Ernst H K Stelzer. “Optical Sectioning Deep Inside Live Embryos by Selective Plane Illumination Microscopy”. In: *Science* 305.5686 (Aug. 2004), pp. 1007–1009.

[42] Misha B Ahrens, Michael B Orger, Drew N Robson, Jennifer M Li and Philipp J Keller. “Whole-brain functional imaging at cellular resolution using light-sheet microscopy”. In: *Nature Methods* 10.5 (May 2013), pp. 413–420.

[43] C Dunsby. “Optically sectioned imaging by oblique plane microscopy”. In: *Optics Express* 16.25 (Dec. 2008), pp. 20306–20316.

[44] Venkatakaushik Voleti, Kripa B Patel, Wenze Li, Citlali Perez Campos, Srinidhi Bharadwaj, Hang Yu, Caitlin Ford, Malte J Casper, Richard Wenwei Yan, Wenxuan Liang, Chentao Wen, Koutarou D Kimura, Kimara L Targoff and Elizabeth M C Hillman. “Real-time volumetric microscopy of in vivo dynamics and large-scale samples with SCAPE 2.0”. In: *Nature Methods* 16.10 (Oct. 2019), pp. 1054–1062.

[45] Xudong Lin, Shiqi Wang, Xudong Yu, Zhuguo Liu, Fei Wang, Wai Tsun Li, Shuk Han Cheng, Qiuyun Dai and Peng Shi. “High-throughput mapping of brain-wide activity in awake and drug-responsive vertebrates”. In: *Lab on a Chip* 15.3 (2015), pp. 680–689.

[46] Manish Kumar and Yevgenia Kozorovitskiy. “Tilt-invariant scanned oblique plane illumination microscopy for large-scale volumetric imaging”. In: *Optics Letters* 44.7 (2019), pp. 1706–4.

[47] Sunil Kumar, Dean Wilding, Markus B Sikkel, Alexander R Lyon, Ken T MacLeod and Chris Dunsby. “High-speed 2D and 3D fluorescence microscopy of cardiac myocytes.” In: *Optics Express* 19.15 (July 2011), pp. 13839–13847.

[48] Markus B Sikkel, Sunil Kumar, Vincent Maioli, Christina Rowlands, Fabiana Gordon, Sian E Harding, Alexander R Lyon, Kenneth T MacLeod and Chris Dunsby. “High speed sCMOS-based oblique plane microscopy applied to the study of calcium dynamics in cardiac myocytes.” In: *Journal of Biophotonics* 9.3 (Mar. 2016), pp. 311–323.

[49] Sunil Kumar, Dean Wilding, Markus B Sikkel, Alexander R Lyon, Ken T MacLeod and Chris Dunsby. “Application of oblique plane microscopy to high speed live cell imaging”. In: *Advanced Microscopy Techniques II*. Ed. by Peter T C So and Emmanuel Beaurepaire. International Society for Optics and Photonics, June 2011, p. 80860V.

[50] Manish Kumar, Sandeep Kishore, Jordan Nasenbeny, David L McLean and Yevgenia Kozorovitskiy. “Integrated one-and two-photon scanned oblique plane illumination (SOPi) microscopy for rapid volumetric imaging”. In: *Optics express* 26.10 (2018), pp. 13027–13041.

[51] Younghoon Shin, Dongmok Kim and Hyuk-Sang Kwon. “Oblique scanning 2-photon light-sheet fluorescence microscopy for rapid volumetric imaging”. In: *Journal of Biophotonics* 11.5 (Feb. 2018), e201700270–8.

[52] Matthew B Bouchard, Venkatakaushik Voleti, CÃ sar S Mendes, Clay Lacefield, Wesley B Grueber, Richard S Mann, Randy M Bruno and Elizabeth M C Hillman. “Swept confocally-aligned planar excitation (SCAPE) microscopy for high-speed volumetric imaging of behaving organisms”. In: *Nature Photonics* (Jan. 2015), pp. 1–7.

[53] Marius Pachitariu, Carsen Stringer, Mario Dipoppa, Sylvia Schröder, L. Federico Rossi, Henry Dalgleish, Matteo Carandini and Kenneth D. Harris. “Suite2p: beyond 10,000 neurons with standard two-photon microscopy”. In: *bioRxiv* (2017). DOI: 10.1101/061507. URL: https://www.biorxiv.org/content/early/2017/07/20/061507.

[54] Rainer W Friedrich, Gilad A Jacobson and Peixin Zhu. “Circuit Neuroscience in Zebrafish”. In: *Current Biology* 20.8 (Apr. 2010), R371–R381.

[55] Christopher M Dooley, Alessandro Mongera, Brigitte Walderich and Christiane Nüsslein-Volhard. “On the embryonic origin of adult melanophores: the role of ErbB and Kit signalling in establishing melanophore stem cells in zebrafish”. In: *Development* 140.5 (2013), pp. 1003–1013.

[56] Ruben Portugues, Claudia E Feierstein, Florian Engert and Michael B Orger. “Whole-Brain Activity Maps Reveal Stereotyped, Distributed Networks for Visuomotor Behavior”. In: *Neuron* 81.6 (Mar. 2014), pp. 1328–1343.

[57] Dal Hyung Kim, Jungsoo Kim, João C Marques, Abhinav Grama, David G C Hildebrand, Wenchao Gu, Jennifer M Li and Drew N Robson. “Pan-neuronal calcium imaging with cellular resolution in freely swimming zebrafish”. In: *Nature Methods* 14.11 (Nov. 2017), p. 1107.

[58] Takashi Kawashima, Maarten F Zwart, Chao-Tsung Yang, Brett D Mensh and Misha B Ahrens. “The Serotonergic System Tracks the Outcomes of Actions to Mediate Short-Term Motor Learning”. In: *Cell* 167.4 (Nov. 2016), 933–946.e20.

[59] Timothy W Dunn, Yu Mu, Sujatha Narayan, Owen Randlett, Eva A Naumann, Chao-Tsung Yang, Alexander F Schier, Jeremy Freeman, Florian Engert and Misha B Ahrens. “Brain-wide mapping of neural activity controlling zebrafish exploratory locomotion”. In: *eLife* 5 (Mar. 2016), p. 471.

[60] João C Marques, Meng Li, Diane Schaak, Drew N Robson and Jennifer M Li. “Internal state dynamics shape brainwide activity and foraging behaviour”. In: *Nature* 577.7789 (Jan. 2020), pp. 239–243.

[61] Martin Haesemeyer, Drew N Robson, Jennifer M Li, Alexander F Schier and Florian Engert. “A Brain-wide Circuit Model of Heat-Evoked Swimming Behavior in Larval Zebrafish”. In: *Neuron* 98.4 (May 2018), 817–831.e6.

[62] Elena I Dragomir, Vilim Štih and Ruben Portugues. “Evidence accumulation during a sensorimotor decision task revealed by whole-brain imaging”. In: *Nature Neuroscience* 23.1 (2020), pp. 85–93.

[63] Carol C Cubbage and Paula M Mabee. “Development of the cranium and paired fins in the zebrafish Danio rerio (Ostariophysi, Cyprinidae)”. In: *Journal of Morphology* 229.2 (Aug. 1996), pp. 121–160.

[64] Lisanne Schulze, Jörg Henninger, Mykola Kadobianskyi, Thomas Chaigne, Ana Isabel Faustino, Nahid Hakiy, Shahad Albadri, Markus Schuelke, Leonard Maler, Filippo Del Bene and Benjamin Judkewitz. “Transparent Danionella translucida as a genetically tractable vertebrate brain model”. In: *Nature Methods* 15.11 (Nov. 2018), pp. 977–983.

[65] E J Botcherby, R Juškaitis, M J Booth and T Wilson. “An optical technique for remote focusing in microscopy”. In: *Optics Communications* 281.4 (Feb. 2008), pp. 880–887.

[66] Maximilian Hoffmann and Benjamin Judkewitz. “Diffractive oblique plane microscopy”. In: *Optica* 6.9 (2019), pp. 1166–1170.

[67] Catherine A McCormick. “Anatomy of the Central Auditory Pathways of Fish and Amphibians”. In: *Comparative Hearing: Fish and Amphibians* 11.Chapter 5 (Jan. 1999), pp. 155–217.

[68] Benedikt Grothe, Catherine E Carr, John H Casseday, Bernd Fritzsch and Christine Köppl. “The Evolution of Central Pathways and Their Neural Processing Patterns”. In: *Evolution of the Vertebrate Auditory System*. New York, NY: Springer, New York, NY, 2004, pp. 289–359.

[69] Deana A Bodnar and Andrew H Bass. “Temporal Coding of Concurrent Acoustic Signals in Auditory Midbrain”. In: *Journal of Neuroscience* 17.19 (Oct. 1997), pp. 7553–7564.

[70] Siegfried Weisenburger, Frank Tejera, Jeffrey Demas, Brandon Chen, Jason Manley, Fraser T Sparks, Francisca Martínez Traub, Tanya Daigle, Hongkui Zeng, Attila Losonczy and Alipasha Vaziri. “Volumetric Ca2+ Imaging in the Mouse Brain Using Hybrid Multiplexed Sculpted Light Microscopy”. In: *Cell* 177.4 (May 2019), 1050–1066.e14.

[71] Lu Xu, Wenze Li, Venkatakaushik Voleti, Dong-Jing Zou, Elizabeth M C Hillman and Stuart Firestein. “Widespread receptor-driven modulation in peripheral olfactory coding”. In: *Science* 368.6487 (Apr. 2020), eaaz5390.

[72] Natalia Orlova, Dmitri Tsyboulski, Farzaneh Najafi, Sam Seid, Sara Kivikas, India Kato, Fiona Griffin, Arielle Leon, Quinn L’Heureux, Kat North, Jackie Swapp, Chelsea Nayan, Nicole Hancock, Ruweida Ahmed, Emily Gelfand, Andrew Cho, Kyla Mace, Robert Howard, Linzy Casal, Sophie Lambert, Eric Kenji Lee, Shiella Caldejon, Xana Waughman, Allison Williford, Marina Garrett, Doug Ollerenshaw, Shawn R. Olsen, Peter Groblewski, Jérôme Lecoq and Peter Saggau. “Multiplane Mesoscope reveals distinct cortical interactions following expectation violations”. In: *bioRxiv* (2020). DOI: 10.1101/2020.10.06.328294. URL: https://www.biorxiv.org/content/early/2020/10/10/2020.10.06.328294.

[73] Vincent Villette, Mariya Chavarha, Ivan K Dimov, Jonathan Bradley, Lagnajeet Pradhan, Benjamin Mathieu, Stephen W Evans, Simon Chamberland, Dongqing Shi, Renzhi Yang, Benjamin B Kim, Annick Ayon, Abdelali Jalil, François St-Pierre, Mark J Schnitzer, Guoqiang Bi, Katalin Toth, Jun Ding, Stéphane Dieudonné and Michael Z Lin. “Ultrafast Two-Photon Imaging of a High-Gain Voltage Indicator in Awake Behaving Mice”. In: *Cell* 179.7 (Dec. 2019), 1590–1608.e23.

[74] K M Naga Srinivas Nadella, Hana Roš, Chiara Baragli, Victoria A Griffiths, George Konstantinou, Theo Koimtzis, Geoffrey J Evans, Paul A Kirkby and R Angus Silver. “Random-access scanning microscopy for 3D imaging in awake behaving animals”. In: *Nature Methods* 13.12 (Dec. 2016), pp. 1001–1004.

[75] Jerome Mertz and Jinhyun Kim. “Scanning light-sheet microscopy in the whole mouse brain with HiLo background rejection”. In: *Journal of Biomedical Optics* 15.1 (2010), pp. 016027–7.

[76] Eugen Baumgart and Ulrich Kubitscheck. “Scanned light sheet microscopy with confocal slit detection”. In: *Optics Express* 20.19 (2012), pp. 21805–21814.

[77] Bin Yang, Alfred Millett-Sikking, Merlin Lange, Ahmet Can Solak, Hirofumi Kobayashi, Andrew York and Loic A. Royer. “High-Resolution, Large Field-of-View, and Multi-View Single Objective Light-Sheet Microscopy”. In: *bioRxiv* (2020). DOI: 10.1101/2020.09.22.309229. URL: https://www.biorxiv.org/content/early/2020/09/24/2020.09.22.309229.

[78] Hugh Sparks, Lucas Dent, Chris Bakal, Axel Behrens, Guillaume Salbreux and Chris Dunsby. “Dual-view oblique plane microscopy (dOPM)”. In: *Biomedical Optics Express* 11.12 (2020), pp. 7204–7220.

[79] Antonia H Groneberg, João C Marques, A Lucas Martins, Ruth Diez del Corral, Gonzalo G de Polavieja and Michael B Orger. “Early-Life Social Experience Shapes Social Avoidance Reactions in Larval Zebrafish”. In: *Current Biology* (Sept. 2020).

[80] Claire Wyart and Vatsala Thirumalai. “Building behaviors, one layer at a time”. In: *eLife* 8 (Apr. 2019), p. 934.

[81] Carmen Diaz Verdugo, Sverre Myren-Svelstad, Ecem Aydin, Evelien Van Hoeymissen, Celine Deneubourg, Silke Vanderhaeghe, Julie Vancraeynest, Robbrecht Pelgrims, Mehmet Ilyas Cosacak, Akira Muto, Caghan Kizil, Koichi Kawakami, Nathalie Jurisch-Yaksi and Emre Yaksi. “Glia-neuron interactions underlie state transitions to generalized seizures”. In: *Nature Communications* 10.1 (Aug. 2019), pp. 1–13.

[82] Ziqiang Wei, Hidehiko Inagaki, Nuo Li, Karel Svoboda and Shaul Druckmann. “An orderly single-trial organization of population dynamics in premotor cortex predicts behavioral variability”. In: *Nature Communications* 10.1 (Jan. 2019), pp. 1–14.

[83] Wenjun Shao, Kivilcim Kilic, Wenqing Yin, Gregory Wirak, Xiaodan qin, Hui Feng, David Boas, Christopher V. Gabel and Ji Yi. “Wide field-of-view volumetric imaging by a mesoscopic scanning oblique plane microscopy with switchable objective lens”. In: *bioRxiv* (2020). DOI: 10.1101/2020.06.29.177782. URL: https://www.biorxiv.org/content/early/2020/06/30/2020.06.29.177782.

[84] Etai Sapoznik, Bo-Jui Chang, Jaewon Huh, Robert J Ju, Evgenia V Azarova, Theresa Pohlkamp, Erik S Welf, David Broadbent, Alexandre F Carisey, Samantha J Stehbens et al. “A versatile Oblique Plane Microscope for large-scale and high-resolution imaging of subcellular dynamics”. In: *Elife* 9 (2020), e57681.

[85] Shannon Fisher, Elizabeth A Grice, Ryan M Vinton, Seneca L Bessling, Akihiro Urasaki, Koichi Kawakami and Andrew S McCallion. “Evaluating the biological relevance of putative enhancers using Tol2 transposon-mediated transgenesis in zebrafish”. In: *Nature protocols* 1.3 (2006), p. 1297.

[86] Andrea Giovannucci, Johannes Friedrich, Pat Gunn, Jeremie Kalfon, Brandon L Brown, Sue Ann Koay, Jiannis Taxidis, Farzaneh Najafi, Jeffrey L Gauthier, Pengcheng Zhou, Baljit S Khakh, David W Tank, Dmitri B Chklovskii and Eftychios A Pnevmatikakis. “CaImAn an open source tool for scalable calcium imaging data analysis”. In: *eLife* 8 (Jan. 2019), p. 413.

C Contributions

Supervision	*Prof. Dr. Benjamin Judkewitz*
Design and Construction of Optical Systems	*Maximilian Hoffmann*
Characterizations of the Optical Systems	*Maximilian Hoffmann*
Imaging of Juvenile and Larval Zebrafish	*Maximilian Hoffmann*
Imaging of *Danionella Translucida*	*Maximilian Hoffmann, Dr. Jörg Henninger*
Data Analysis	*Maximilian Hoffmann*
Neural Anatomy of *Danionella translucida*	*Maximilian Hoffmann, Dr. Jörg Henninger*

Eidesstattliche Versicherung

„Ich, Maximilian Hoffmann, versichere an Eides statt durch meine eigenhändige Unterschrift, dass ich die vorgelegte Dissertation mit dem Thema: **Neuartige Einzelobjektiv-Lichtblattmikroskope für optisches Neuroimaging ganzer Gehirne von Bärblingen** / **Novel Oblique Plane Microscopes for Whole-Brain Imaging of Danionins** selbstständig und ohne nicht offengelegte Hilfe Dritter verfasst und keine anderen als die angegebenen Quellen und Hilfsmittel genutzt habe.
Alle Stellen, die wörtlich oder dem Sinne nach auf Publikationen oder Vorträgen anderer Autoren/innen beruhen, sind als solche in korrekter Zitierung kenntlich gemacht. Die Abschnitte zu Methodik (insbesondere praktische Arbeiten, Laborbestimmungen, statistische Aufarbeitung) und Resultaten (insbesondere Abbildungen, Graphiken und Tabellen) werden von mir verantwortet.

Ich versichere ferner, dass ich die in Zusammenarbeit mit anderen Personen generierten Daten, Datenauswertungen und Schlussfolgerungen korrekt gekennzeichnet und meinen eigenen Beitrag sowie die Beiträge anderer Personen korrekt kenntlich gemacht habe (siehe Anteilserklärung). Texte oder Textteile, die gemeinsam mit anderen erstellt oder verwendet wurden, habe ich korrekt kenntlich gemacht.

Meine Anteile an etwaigen Publikationen zu dieser Dissertation entsprechen denen, die in der untenstehenden gemeinsamen Erklärung mit dem/der Erstbetreuer/in, angegeben sind. Für sämtliche im Rahmen der Dissertation entstandenen Publikationen wurden die Richtlinien des ICMJE (International Committee of Medical Journal Editors; www.icmje.og) zur Autorenschaft eingehalten. Ich erkläre ferner, dass ich mich zur Einhaltung der Satzung der Charité – Universitätsmedizin Berlin zur Sicherung Guter Wissenschaftlicher Praxis verpflichte.

Weiterhin versichere ich, dass ich diese Dissertation weder in gleicher noch in ähnlicher Form bereits an einer anderen Fakultät eingereicht habe.

Die Bedeutung dieser eidesstattlichen Versicherung und die strafrechtlichen Folgen einer unwahren eidesstattlichen Versicherung (§§156, 161 des Strafgesetzbuches) sind mir bekannt und bewusst.“

Datum Unterschrift

Ausführliche Anteilserklärung an der erfolgten Publikation als Top-Journal im Rahmen der Promotionsverfahren zum PhD bzw. MD/PhD.

Publikation 1:

Hoffmann, Maximilian, & Judkewitz, Benjamin, Diffractive oblique plane microscopy, Optica, 6(9), 1166–1170, (2019).

Beitrag im Einzelnen:
Das Forschungsprojekt wurde in Zusammenarbeit mit meinem erstbetreuenden Hochschullehrer Benjamin Judkewitz entwickelt. Darüber hinaus habe ich alle Aspekte des Projekts eingenständig durchgeführt: Ich habe das Mikroskop entwickelt, konzipiert, und gebaut. Des Weiteren habe ich die Kontrollsoftware und Datenpreprocessing-Software geschrieben. Ich habe die Charakterisierung des optischen Systems übernommen, sowie die Neuroimaging Experimente mit juvenile Zebrafischen und Zebrafishlarven durchgeführt. Zudem habe ich die Datenanalyse der experimentellen Daten durchgeführt. Das Manuskript der Publikation 1 wurde in Zusammenarbeit mit meinem erstbetreuenden Hochschullehrer Benjamin Judkewitz geschrieben.

_____
Unterschrift, Datum und Stempel des/der erstbetreuenden Hochschullehrers/in

_____
Unterschrift des Doktoranden/der Doktorandin

Journal Data Filtered By: **Selected JCR Year: 2017** Selected Editions: SCIE,SSCI Selected Categories: **"OPTICS"** Selected Category Scheme: WoS

Gesamtanzahl: 94 Journale

Rank	Full Journal Title	Total Cites	Journal Impact Factor	Eigenfactor Score
1	Nature Photonics	39,331	32.521	0.128020
2	Advances in Optics and Photonics	2,050	21.286	0.004820
3	Light-Science & Applications	4,249	13.625	0.015690
4	Laser & Photonics Reviews	5,403	8.529	0.016740
5	Optica	4,366	7.536	0.023710
6	Advanced Optical Materials	5,612	7.430	0.020250
7	ACS Photonics	5,823	6.880	0.024530
8	Nanophotonics	1,196	6.014	0.005120
9	Progress in Optics	988	5.545	0.000690
10	Photonics Research	1,208	5.242	0.003990
11	Neurophotonics	533	4.129	0.002070
12	Journal of Biophotonics	2,723	3.768	0.006190
13	JOURNAL OF LIGHTWAVE TECHNOLOGY	22,458	3.652	0.030050
14	OPTICS LETTERS	66,148	3.589	0.103500
15	Biomedical Optics Express	8,120	3.482	0.022730
16	Advances In Atomic Molecular and Optical Physics	864	3.450	0.001290
17	OPTICS AND LASERS IN ENGINEERING	6,479	3.388	0.008670
18	IEEE JOURNAL OF SELECTED TOPICS IN QUANTUM ELECTRONICS	9,476	3.367	0.014000
19	OPTICS EXPRESS	104,686	3.356	0.192190
20	JOURNAL OF SYNCHROTRON RADIATION	6,027	3.232	0.012400
21	High Power Laser Science and Engineering	317	3.143	0.001380

22	IEEE Transactions on Terahertz Science and Technology	1,878	2.955	0.006540
23	PHYSICAL REVIEW A	110,542	2.909	0.166870
24	Journal of Optical Communications and Networking	2,340	2.742	0.005390
25	JOURNAL OF LUMINESCENCE	17,185	2.732	0.019800
26	Journal of Astronomical Telescopes Instruments and Systems	307	2.688	0.000870
27	IEEE Photonics Journal	5,269	2.627	0.014730
28	JOURNAL OF QUANTITATIVE SPECTROSCOPY & RADIATIVE TRANSFER	10,480	2.600	0.012750
29	Leukos	373	2.576	0.000760
30	Optical Materials Express	4,773	2.566	0.012720
31	OPTICS AND LASER TECHNOLOGY	5,914	2.503	0.010030
32	IEEE PHOTONICS TECHNOLOGY LETTERS	16,907	2.446	0.024040
33	EPJ Quantum Technology	152	2.436	0.001000
34	JOURNAL OF BIOMEDICAL OPTICS	13,503	2.367	0.019530
35	Journal of Optics	4,851	2.323	0.014700
36	OPTICAL MATERIALS	11,471	2.320	0.013930
37	LASER PHYSICS LETTERS	3,717	2.235	0.008260
38	IMAGE AND VISION COMPUTING	5,280	2.159	0.005250
39	Journal of Photonics for Energy	495	2.157	0.001200
40	JOURNAL OF PHYSICS B-ATOMIC MOLECULAR AND OPTICAL PHYSICS	13,405	2.119	0.019830
41	IEEE JOURNAL OF QUANTUM ELECTRONICS	9,136	2.069	0.004330
42	JOURNAL OF THE OPTICAL SOCIETY OF AMERICA B-OPTICAL PHYSICS	12,830	2.048	0.015290

43	MICROELECTRONIC ENGINEERING	8,183	2.020	0.009490
44	Chinese Optics Letters	2,542	1.948	0.003770
45	Lighting Research & Technology	1,393	1.921	0.001570
46	OPTICS COMMUNICATIONS	21,801	1.887	0.022170
47	APPLIED PHYSICS B-LASERS AND OPTICS	10,704	1.881	0.013160
48	INFRARED PHYSICS & TECHNOLOGY	3,572	1.851	0.004560
49	APPLIED OPTICS	45,131	1.791	0.038230
50	Journal of Infrared Millimeter and Terahertz Waves	1,457	1.677	0.003760
51	JOURNAL OF LASER APPLICATIONS	1,040	1.597	0.001760
52	Photonics and Nanostructures-Fundamentals and Applications	700	1.575	0.001640
53	JOURNAL OF THE OPTICAL SOCIETY OF AMERICA A-OPTICS IMAGE SCIENCE AND VISION	13,980	1.566	0.010950
54	INTERNATIONAL JOURNAL OF PHOTOENERGY	2,956	1.547	0.006150
55	IET Optoelectronics	330	1.506	0.000610
56	JOURNAL OF NONLINEAR OPTICAL PHYSICS & MATERIALS	573	1.491	0.000530
57	INTERNATIONAL JOURNAL OF IMAGING SYSTEMS AND TECHNOLOGY	690	1.423	0.001030
58	EUROPEAN PHYSICAL JOURNAL D	4,837	1.393	0.007450
59	Journal of X-Ray Science and Technology	646	1.381	0.000940
60	OPTICAL FIBER TECHNOLOGY	1,709	1.350	0.002660
61	Photonic Sensors	491	1.317	0.000800
62	Journal of Micro-Nanolithography MEMS and MOEMS	972	1.299	0.001710
63	JOURNAL OF MODERN OPTICS	4,686	1.269	0.004600

64	Journal of the European Optical Society-Rapid Publications	598	1.250	0.001360
65	PHOTONIC NETWORK COMMUNICATIONS	476	1.203	0.000870
66	OPTIK	8,821	1.191	0.013550
67	DISPLAYS	986	1.175	0.000990
68	OPTICAL AND QUANTUM ELECTRONICS	2,555	1.168	0.003500
69	LASER PHYSICS	2,835	1.158	0.004310
70	OPTO-ELECTRONICS REVIEW	743	1.156	0.000710
71	Journal of Innovative Optical Health Sciences	418	1.136	0.000650
72	Optical Switching and Networking	363	1.113	0.000670
73	Journal of the Society for Information Display	1,069	1.102	0.001220
74	Journal of Nanophotonics	886	1.060	0.001650
75	OPTICAL ENGINEERING	9,341	0.993	0.009740
76	MICROWAVE AND OPTICAL TECHNOLOGY LETTERS	5,946	0.948	0.007500
77	OPTICA APPLICATA	586	0.925	0.000530
78	FIBER AND INTEGRATED OPTICS	257	0.895	0.000180
79	International Journal of Optomechatronics	164	0.882	0.000300
80	OPTICS AND SPECTROSCOPY	2,911	0.824	0.002280
81	OPTICAL REVIEW	828	0.805	0.001110
82	Journal of Laser Micro Nanoengineering	500	0.789	0.000720
83	JOURNAL OF ELECTRONIC IMAGING	1,924	0.780	0.002580
84	Journal of the Optical Society of Korea	528	0.637	0.001030
85	JOURNAL OF RUSSIAN LASER RESEARCH	373	0.553	0.000450
86	Ukrainian Journal of Physical Optics	114	0.488	0.000150

87	JOURNAL OF OPTICAL TECHNOLOGY	762	0.392	0.000610
88	JOURNAL OF OPTOELECTRONICS AND ADVANCED MATERIALS	2,045	0.390	0.000820
89	JOURNAL OF INFRARED AND MILLIMETER WAVES	397	0.387	0.000340
90	Optoelectronics and Advanced Materials-Rapid Communications	922	0.386	0.000980
91	LASERS IN ENGINEERING	215	0.305	0.000320
92	Light & Engineering	94	0.160	0.000090
93	LASER FOCUS WORLD	175	0.151	0.000220
94	Current Optics and Photonics	5	Not Available	0.000000

D Manuscript

Research Article Vol. 6, No. 9 / September 2019 / Optica 1166

Diffractive oblique plane microscopy

MAXIMILIAN HOFFMANN AND BENJAMIN JUDKEWITZ*

Charité Universitätsmedizin Berlin, Einstein Center for Neurosciences, NeuroCure Cluster of Excellence, Charitéplatz 1, 10117 Berlin, Germany
**Corresponding author: benjamin.judkewitz@charite.de*

Received 26 March 2019; revised 12 July 2019; accepted 12 July 2019 (Doc. ID 363426); published 3 September 2019

Imaging of neuronal activity with fluorescent indicators is an important technique in neuroscience. However, it remains challenging to record volumetric image data at fast frame rates and good resolution. One promising technique to achieve this goal is light sheet microscopy (LSM), but the right angle configuration of the excitation and imaging system limits its application. Oblique plane microscopy (OPM), a variant of LSM, circumvents this limitation by exciting oblique planes and detecting the image through the same microscope objective lens. So far, these techniques have relied on the use of high numerical aperture (NA) detection objective lenses, which limits their field of view. Here we present an OPM technique that allows for the use of low NA objective lenses by redirecting the light with the help of a diffraction grating. The microscope maintains a micrometer-scale lateral resolution over a large addressable imaging volume of 3.3 × 3.0 × 1.0 mm^3. We demonstrate its practicality by imaging the whole brain of larval and juvenile zebrafish.

https://doi.org/10.1364/OPTICA.6.001166

1. INTRODUCTION

Optical recording of neural activity has become an essential part of neuroscientific research. One of the most widely used techniques, two-photon microscopy [1], has an excellent resolution, is resilient to scattering tissue, and can record from a large field of view (FOV) [2,3], but its sequential detection scheme and the fluorescence lifetime limit the amount of neurons per unit of time it can record from. A number of techniques have thus been developed to increase volumetric imaging speed. Some techniques try to increase the excitation spot size of the two-photon scanning microscope [4,5], therefore reducing the number of points that have to be sampled. This enables faster acquisition rates from a given volume, but fundamentally remains subject to the limitations imposed by sequential detection. Other optical techniques achieve volumetric recordings by capturing a single snapshot on a camera sensor and thereby circumvent the limitations of sequential scanning schemes. This is achieved by multi-aperture imaging combined with computational reconstruction, as in light field microscopy [6–10] or by multiplexing and focusing different focal planes onto different sensor areas with the help of diffractive optics [11–13]. These camera-based techniques employ one-photon excitation, since the requirements on the total power of the light source as well as on the maximal permissive energy flux into the specimen can be more easily met. This sacrifices the confinement of the excitation volume of non-linear microscopy and leads to the loss of any optical sectioning capability, understood here as the "missing cone" in the 3D optical transfer function of the microscope [14]. One way to guarantee optical sectioning in linear microscopy is to break the collinearity of emission and excitation point spread functions (PSFs) as in light sheet microscopy or selective plane illumination microscopy (LSM/SPIM) techniques [15–17]. In LSM/SPIM, a light sheet perpendicular to the imaging objective excites the imaging plane. The excited fluorescence from an entire plane is then imaged onto a camera sensor by an imaging system situated at a right angle to the excitation beam. This requires the specimen to be accessible and optically transparent on both the imaging side as well as on the perpendicular excitation side, which is often not possible due to the cranium or other anatomical features of the organism of interest, such as the eyes in the case of fish.

Oblique plane microscopy (OPM) techniques circumvent these geometrical constraints by realizing lightsheet-type excitation and imaging through the same objective lens on oblique planes [18–26]. As a result, they require access to the sample from one side only (e.g., the top of the head for neuronal imaging). Exciting tilted planes decreases the angle between emission and excitation PSF [Fig. 1(a)], but still enables optical sectioning. For volumetric imaging, the oblique excitation sheet is scanned while the emitted light is descanned onto an oblique intermediate image plane. A high-speed OPM technique termed SCAPE achieves this with fast scanning mirrors and has been used to image neuronal calcium signals in mice and in larval Drosophila [21,27]. To avoid spherical aberrations associated with imaging of oblique planes, OPM methods employ a one-to-one magnification system [28]. The oblique intermediate image plane is then brought to lie perpendicular to the optical axis of a tertiary imaging system and can be captured in a conventional way by a camera. To maintain the FOV of the primary imaging system, the third objective lens has to have the same or lower NA, because optical design restrictions lead to an inverse relationship between objective NA and attainable FOV. This reimaging geometry inherently leads to losses, as parts of the light will not propagate

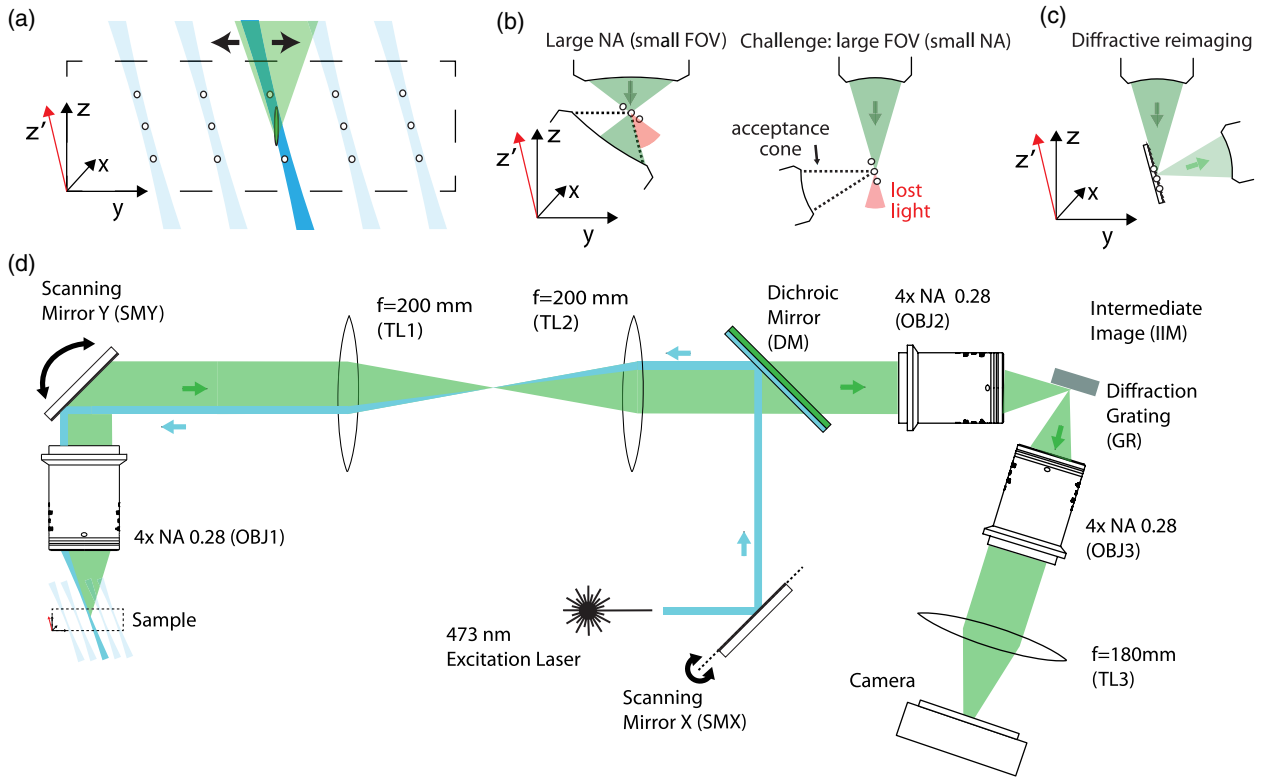

Fig. 1. Principle of operation. (a) Recording geometry of oblique plane microscopy: a swept Gaussian laser beam (dark blue) excites an oblique plane within the specimen (dashed box); the optical section is the result of the angle between the detection point spread function (PSF, green ellipsoid) and the excitation PSF (Gaussian beam). The emitted fluorescence light within the acceptance angle (green cone) is captured by the objective. Volumetric imaging is achieved by scanning the excitation light to parallel planes (light blue). The white circles represent sample points on the sheared volumetric grid and successive camera images. (b) Oblique reimaging for two different numerical apertures: an intermediate image plane (circles) is created and reimaged by two identical objectives. A part of the light cone emerging from the first objective (green) is not collected (red) because it does not propagate within the acceptance angle of the second objective. As the numerical aperture (NA) decreases, the light is completely lost. (c) Diffractive oblique reimaging: the inserted diffraction grating diffracts parts of the light into a direction almost perpendicular to the grating and allows reimaging at low NA. The angle of the grating matches the angles of the imaging planes in (b). (d) Setup: the laser focus at the galvanometric scanning mirror (SMX) is imaged onto a decentered spot at the backfocal aperture of the imaging objective OBJ1 by the $4f$ system consisting of the two tube lenses TL1 and TL2. This leads to an oblique incidence at the sample. Scanning the mirror SMX excites fluorescence in an oblique plane. The emitted fluorescence from the oblique plane is imaged onto a blazed diffraction grating (GR) at the intermediate image plane (IIM) with unit magnification by means of two identical imaging systems (OBJ1 TL1, OBJ2 TL2). The surface of the diffraction grating (GR) is imaged by a third imaging system (OBJ3, TL3) place perpendicular to the grating surface. The third imaging system collects the diffracted fluorescence at the IIM and images it onto the camera. A volume is imaged by scanning and descanning the imaging plane in the sample by scanning the galvanometric scanning mirror SMY.

inside the acceptance angle of the tertiary objective lens [Fig. 1(b)]. The loss becomes total at an NA ≤ 0.5 and prohibits the use of low-NA objectives, which are needed for large-FOV imaging. This has so far limited the FOV of OPM to $\leq 1 \times 1$ mm^2 [21,29].

Here, we overcome this limitation by employing a diffraction grating to allow oblique reimaging for low-NA objectives [30] and therefore enable OPM across a large FOV of 3.3×3.0 mm^2 [Fig. 1(c)].

2. METHOD

Our optical setup is schematically summarized in Fig. 1(d). Two identical imaging systems consisting of an imaging objective lens (XLFluor, 4 ×, 0.28 NA, corrected for a water layer of 0–5 mm, Olympus, used as OBJ1 and OBJ2) and a telecentric tube lens (TTL200MP, $f = 200$ mm, Thorlabs, used as TL1 and TL2) are placed back to back in order to create an intermediate image of the sample at the intermediate image plane (IIM). Here, OBJ1 carries an immersion cap (not shown), which establishes a stable contact surface to the water-embedded specimen. Our imaging system thus creates an intermediate image of the object with a lateral magnification $M_{\mathrm{lat}} = 1$ and an axial magnification $M_{\mathrm{ax}} = n_{\mathrm{air}}/n_{\mathrm{water}} = 0.75$.

To excite fluorescence within the specimen, excitation light is generated by a 473 nm laser (MBL-FN-473-100, CNI Laser), which is coupled into a single-mode fiber and collimated by an aspheric lens (F240APC-532, Thorlabs) to create a Gaussian beam with a waist of 10 μm in the specimen. This results in a theoretical confocal parameter, twice the Rayleigh length, of 954 μm. The laser beam is then directed onto a galvanometric scanning mirror (6 mm, 8315 K, Cambridge Technology, SMX), which is placed at the Fourier plane of the second imaging system. Being reflected of a dichroic mirror

(DM), the galvanometric mirror surface is then imaged onto an off-center point at the back focal aperture of the primary imaging objective (OBJ1). This point is chosen to be maximally displaced from the optical axis while preventing occlusion of the excitation beam. For the NA of 0.28 used here, this beam then exits OBJ1 at the corresponding oblique angle of 14.6° (in air, corresponding to 10.9° in water) and can be used to excite fluorescence in an oblique plane by quickly ramping the scanning mirror SMX.

To translate the excited plane through the specimen, we adopt a strategy similar to that used in Refs. [21,25] and use a scanning mirror to scan the excitation light while descanning the emission light.

In our case, the first imaging system contains a large-aperture galvanometric mirror (25 mm beam diameter, 6240H, Cambridge Technology, SMY), which is placed as close as possible to the back focal plane of the objective lens. This imaging geometry leads to an angle of about 14.6° between the emission and the excitation PSF [Fig. 1(b)]. It also leads to the familiar non-rectilinear coordinate system (xyz') of OPM [25], which can be transformed into a conventional coordinate system via an affine transformation consisting of scaling and shearing [Fig. 1(b), Supplement 1].

Because the emission light is descanned, every plane of excited fluorescence is always reimaged onto the same oblique plane at the IIM, which in conventional OPMs is reimaged onto a camera in transmission by a tilted tertiary imaging system. If both systems have the same NA, this inherently leads to the loss of signal, since some of the light propagates outside of the acceptance angle of the tertiary imaging system [Fig. 1(b)]. This problem only gets worse with lower-NA objective lenses and leads to a total loss of all signal at an NA ≤ 0.5. For large-FOV, low-NA objectives such as the 0.28 NA objective used here, the conventional solution to reimaging is therefore inapplicable [Fig. 1(c)].

To enable the reimaging of an oblique plane formed by a low-NA objective lens, we introduced a reflective blazed grating at the intermediate image plane and aligned it to be coplanar with the image of the oblique fluorescence plane [Figs. 1(a) and 1(c)].

Therefore, every point emitter in the excited plane will be imaged and thus focused onto a point on the grating surface. This light focus is then diffracted into multiple orders, emerging at different directions, which can be approximated by the grating equation

$$(m\lambda/d - \sin(\alpha)) = \sin(\beta).$$

In our case, $\lambda = 510$ nm is the central emission wavelength of eGFP, $\alpha = (90 - 14.6)°$ is the incidence angle, β is the diffraction angle with respect to the grating normal, d is the grating period, and m is an integer.

Given these parameters, we chose a commercially available grating with period $d = 555$ nm (GR, Richardson 33025FL01-290R, 26.7° blaze, 1800/mm), which resulted in three allowed diffraction orders $m = -2, -1, 0$ predicted at $\beta = -60.4$, 2.8, and 75.4°, of which the $m = -1$ diffraction order was measured to carry 43% (at $\lambda = 532$ nm) of the incident light. Since the diffracted light in this order propagated almost perpendicularly to the grating, it could now be captured [Fig. 1(d)] by a tertiary imaging system with the identical NA as the reimaging system. The tertiary imaging system consisted of an objective (OBJ3, XLFluor 4×, 0.28 NA) and a tube lens (TL3, TTL 180-A), which imaged the IIM on the grating surface onto a camera (ORCA-Flash4.0 V2, Hamamatsu). We note that although the diffraction grating was a dispersive element, no additional chromatic aberrations were introduced, since the grating surface was imaged directly onto the camera sensor plane (Supplement 1). The camera sensor contained 2048 × 2048 pixels with a pixel pitch of 6.5 µm. We used a region of 2048 × 616 pixels, which corresponded to an effective FOV of 3328 µm (X) × 1001 µm (Z′) at the grating plane. This matched the confocal parameter and approximate axial imaging range of the Gaussian excitation beam. Furthermore, it allowed us to increase the permissible frame rate to 333 Hz. For volumetric imaging, this image plane could be scanned by ±1500 µm in y with help of SMY, resulting in an accessible imaging volume of 3.3 mm × 3.0 mm × 1.0 mm (X × Y × Z).

3. RESULTS

To characterize the optical system, we first imaged a sample of fluorescent beads (diameter 1 µm) dispersed in agarose and recorded images of beads throughout the whole accessible imaging volume [Fig. 2(a)]. Choosing the distance (along y) between the imaging planes to match the effective pixel size of our camera resulted in an isotropic voxel size of 1.625 µm. Example images at increasing distances from the center of the imaging FOV are shown in Fig. 2(b) and exhibit a constant image quality. We then quantified the lateral resolution of our system by calculating the full width at half maximum (FWHM) of the line sections through maximum intensity projections of each bead. The average FWHM values across the FOV were 2.6 ± 1.6 (x) and 3.1 ± 1.8 µm (y). To determine the axial sectioning capability, we

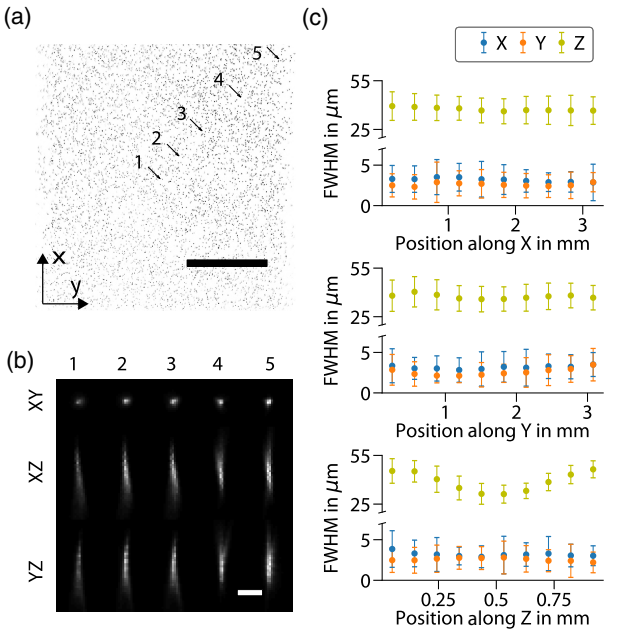

Fig. 2. Quantification of system resolution. (a) Beads in full FOV, maximum intensity projection of bead volume after shear transformation (ST), scale bar 1000 µm. (b) Example beads, maximum intensity projections of five 1 µm sized beads along x, y, and z after ST; the location in the total FOV is indicated by the arrows in (a), scale bar 20 µm. (c) Resolution across the FOV; each plot shows the dependency of the resolution (mean ± SD) along x, y, and z on bead position along x, y, and z (top to bottom).

measured the average FWHM of the axial energy distribution of the microsphere images, calculated as the sum of all pixel values along the *xy* planes of a bead volume and found it to be 37.4 ± 8.4 μm ($n = 3432$). This was constant throughout the FOV, but changed as expected with axial distance from the native image plane due to the broadening of the excitation beam [Fig. 2(c)]. A rough estimate of the information throughput of this imaging configuration can be obtained by dividing its accessible FOV of 3.3 mm × 3.0 mm × 1.0 mm by its volumetric resolution ($2.6 \times 3.1 \times 37.4$ μm^3), resulting in 3.5×10^7 resolvable image points. The data throughput of our microscope is limited by the speed of the camera and can be approximated by the amount of resolvable points in one camera frame (3.3 mm × 1.0 mm/(2.6 μm × 37 μm)) multiplied by the maximum frame rate (333 Hz) to yield 11.1 million samples per second (MS/s). To show that we can consistently capture neuronal activity throughout this imaging volume, we recorded the time changing fluorescence of neurons in a restrained zebrafish larva (elavl3:H2B-GCaMP6s, 4 dpf). We translated it to 3 × 3 different extreme points in the FOV [Fig. 3(a)]. At each position, we recorded a time series of the region containing the entire larva ($3328 \times 382 \times 1001$ μm^3, 191 planes) at a volume rate of 1.75 Hz and were able to record neural activity. [Fig. 3(b), Supplement 1, Visualization 1]. As a second demonstration, we also imaged the time-dependent fluorescent changes of neurons throughout an entire juvenile zebrafish (elavl3:H2B-GCaMP6s, 33 dpf), an age at which conventional LSM would be challenging due to shadowing effects caused by the eyes and developing skull. We recorded a time series of a 3328 μm × 812 μm × 1001 μm volume, containing the whole fish brain. [s. Fig. 3(b)] Within this volume, we recorded 406 planes at a 2 μm spacing. This enabled us to record from 997 neurons at a volume rate of 0.8 Hz [Figs. 3(d) and 3(e), Supplement 1, Visualization 2].

4. DISCUSSION

The microscope design presented in this paper enables fast volumetric recording of neural activity throughout a volume of 3.3 × 3 × 1.0 mm^3 by capturing imaging data from 333 tilted planes per second. The increase in accessible imaging volume in comparison to previously reported OPM techniques [18–25] is an order of magnitude. We achieve this by using a low-NA objective and modification of the central reimaging step of OPM with the help of a diffraction grating.

While allowing for the use of low-NA objectives with increased FOV, our current implementation has an upper limit for the NA. With two objectives on the same side of a reflective grating, geometrical constraints would limit the maximum possible NA to 0.71 (sin 45°). If desired, this limitation could be overcome by using transmission gratings.

Compared to other OPM techniques, we are trading off photon efficiency and resolution for FOV and flexibility, but there are several ways to improve those quantities (Supplement 1). The efficiency could be further increased by transitioning to a custom-designed 0.5 NA objective lens with a FOV similar to those designed and used in Refs. [2,3]. This would simultaneously increase the resolution, the sectioning capability, and the system bandwidth, allowing it to capture more distinct axial planes. Additionally, the efficiency could be increased by a more efficient

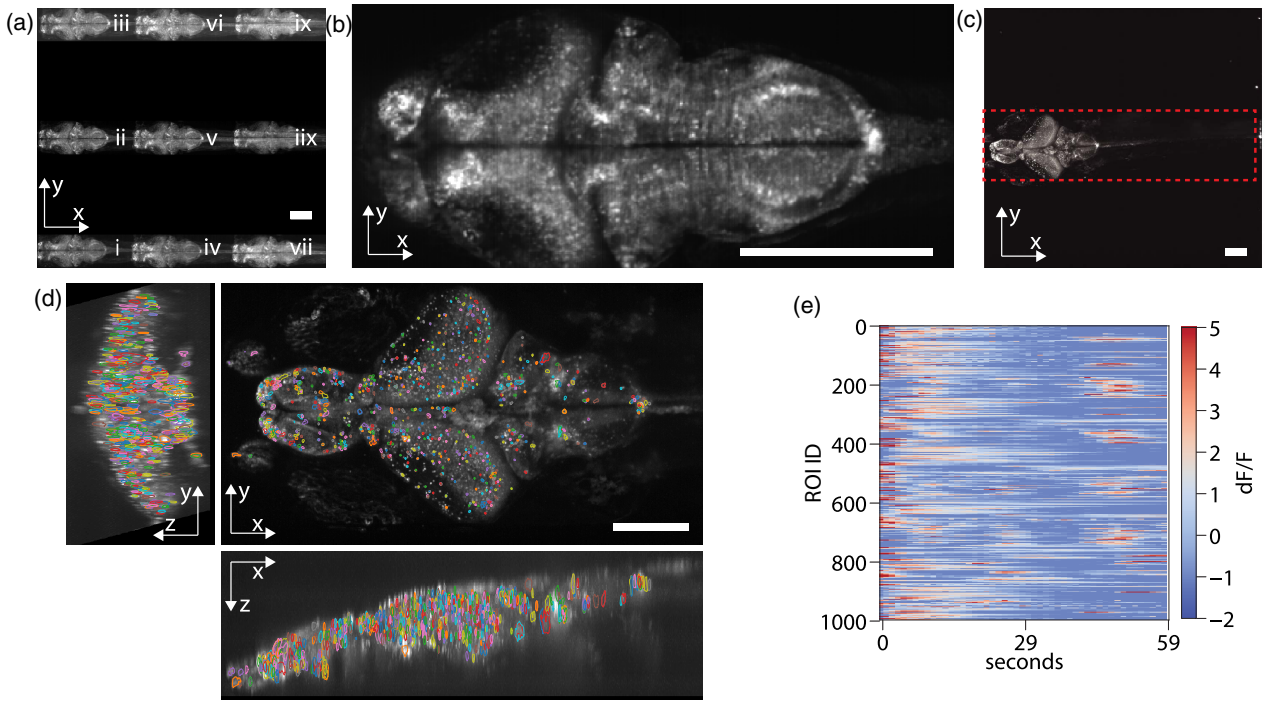

Fig. 3. Measurement of neuronal activity over a large field of view (FOV). (a) Larval zebrafish at different locations across the accessible FOV: montage of a restrained 4dpf Huc:GCaMP6s nuclear zebrafish larva sequentially imaged at nine different locations within the accessible FOV [maximum intensity projection (MIP)]; see Supplement 1, Visualization 1. (b) Slice of the larval zebrafish brain at 100 μm depth and location v. (c) MIP of a 33 dpf Huc:GCaMP6s in the accessible microscope FOV, which was recorded in the time lapse experiments. The dashed red box represents the imaged region. (d) MIP of the brain with overlayed contours of the regions of interest along all three dimensions of the volume; see Supplement 1, Visualization 2. (e) Extracted temporal dF/F traces of the regions of interest shown in (d); scale bar in (a), (b), (c), (d) 250 μm.

diffractive surface. Last, the speed of the technique is currently limited only by the camera speed, but could be increased by implementing a more suitable sampling scheme. Since our microscope captures oblique planes [the xz slice in Fig. 2(b)], a Nyquist sampling along the shorter dimension x leads to a redundant sampling along z. By employing anamorphic optics in the tertiary imaging step, the image could be transformed so that both dimensions are exactly sampled at the Nyquist criterion by the quadratic pixel grid of the camera. This would cut down on the number of acquired pixels per frame and would enable recordings at higher frame rates. This tailored sampling scheme, combined with faster, sensitive cameras, will further increase the sampling rate of this technique.

5. CONCLUSION

Diffractive OPM introduces a new solution for the central reimaging geometry in OPM. It extends the family of these techniques to larger FOVs, and although its resolution is reduced by the use of low-NA objectives, the technique retains OPM's key advantages, such as high speed, a partially parallel detection scheme, true optical sectioning, and a dynamically adjustable region of interest.

Funding. Human Frontier Science Program (HFSP) (RGP0027/2016); H2020 European Research Council (ERC) (ERC-2016-StG-714560); Alfried Krupp von Bohlen und Halbach-Stiftung.

Acknowledgment. We thank Spencer Smith, Thomas Chaigne, Ioannis N. Papadopoulos, Roarke Horstmayer, and Mykola Kadobianskyi for helpful discussions and for critically reading the paper.

See Supplement 1 for supporting content.

REFERENCES

1. W. Denk, J. H. Strickler, and W. W. Webb, "Two-photon laser scanning fluorescence microscopy," Science **248**, 73–76 (1990).
2. J. N. Stirman, I. T. Smith, M. W. Kudenov, and S. L. Smith, "Wide field-of-view, multi-region, two-photon imaging of neuronal activity in the mammalian brain," Nat. Biotechnol. **34**, 857–862 (2016).
3. N. J. Sofroniew, D. Flickinger, J. King, and K. Svoboda, "A large field of view two-photon mesoscope with subcellular resolution for in vivo imaging," eLife **5**, 413 (2016).
4. R. Prevedel, A. J. Verhoef, A. J. Pernía-Andrade, S. Weisenburger, B. S. Huang, T. Nöbauer, A. Fernández, J. E. Delcour, P. Golshani, A. Baltuska, and A. Vaziri, "Fast volumetric calcium imaging across multiple cortical layers using sculpted light," Nat. Methods **13**, 1021–1028 (2016).
5. R. Lu, W. Sun, Y. Liang, A. Kerlin, J. Bierfeld, J. D. Seelig, D. E. Wilson, B. Scholl, B. Mohar, M. Tanimoto, M. Koyama, D. Fitzpatrick, M. B. Orger, and N. Ji, "Video-rate volumetric functional imaging of the brain at synaptic resolution," Nat. Neurosci. **20**, 620–628 (2017).
6. M. Levoy, R. Ng, A. Adams, M. Footer, and M. Horowitz, "Light field microscopy," ACM Trans. Graph. **25**, 924–934 (2006).
7. M. Broxton, L. Grosenick, S. Yang, N. Cohen, A. Andalman, K. Deisseroth, and M. Levoy, "Wave optics theory and 3-D deconvolution for the light field microscope," Opt. Express **21**, 25418–25422 (2013).
8. R. Prevedel, Y.-G. Yoon, M. Hoffmann, N. Pak, G. Wetzstein, S. Kato, T. Schrödel, R. Raskar, M. Zimmer, E. S. Boyden, and A. Vaziri, "Simultaneous whole-animal 3D imaging of neuronal activity using light-field microscopy," Nat. Methods **11**, 727–730 (2014).
9. T. Nöbauer, O. Skocek, A. J. Pernía-Andrade, L. Weilguny, F. M. Traub, M. I. Molodtsov, and A. Vaziri, "Video rate volumetric Ca2+ imaging across cortex using seeded iterative demixing (SID) microscopy," Nat. Methods **14**, 811–818 (2017).
10. L. Cong, Z. Wang, Y. Chai, W. Hang, C. Shang, W. Yang, L. Bai, J. Du, K. Wang, and Q. Wen, "Rapid whole brain imaging of neural activity in freely behaving larval zebrafish (Danio rerio)," eLife **6**, e28158 (2017).
11. S. Abrahamsson, J. Chen, B. Hajj, S. Stallinga, A. Y. Katsov, J. Wisniewski, G. Mizuguchi, P. Soule, F. Mueller, C. D. Darzacq, X. Darzacq, C. Wu, C. I. Bargmann, D. A. Agard, M. Dahan, and M. G. L. Gustafsson, "Fast multicolor 3D imaging using aberration-corrected multifocus microscopy," Nat. Methods **10**, 60–63 (2013).
12. A. Agostinho, A. Jost, D. C. Jans, H. Blom, H. Brismar, K. Bernhem, L. Nilsson, M. Müller, R. Heintzmann, S. Abrahamsson, and T. J. Lambert, "Multifocus structured illumination microscopy for fast volumetric super-resolution imaging," Biomed. Opt. Express **8**, 4135–4140 (2017).
13. B. Hajj, B. Mehl, C. Wu, C. Cho, C. I. Bargmann, J. A. Liddle, J. Wisniewski, J.-B. Fiche, J. Pulupa, L. Oudjedi, L. Chen, L. Yu, M. Davanco, M. Nollmann, M. Dahan, M. El Beheiry, M. Mir, R. Ilic, S. Abrahamsson, T. Lionnet, X. Darzacq, and X. Jin, "Multifocus microscopy with precise color multi-phase diffractive optics applied in functional neuronal imaging," Biomed. Opt. Express **7**, 855–869 (2016).
14. J. Mertz, *Introduction to Optical Microscopy* (Roberts Publishers, 2010).
15. P. J. Keller, A. D. Schmidt, J. Wittbrodt, and E. H. K. Stelzer, "Reconstruction of zebrafish early embryonic development by scanned light sheet microscopy," Science **322**, 1065–1069 (2008).
16. M. B. Ahrens, M. B. Orger, D. N. Robson, J. M. Li, and P. J. Keller, "Whole-brain functional imaging at cellular resolution using light-sheet microscopy," Nat. Methods **10**, 413–420 (2013).
17. J. Huisken, J. Swoger, F. Del Bene, J. Wittbrodt, and E. H. Stelzer, "Optical sectioning deep inside live embryos by selective plane illumination microscopy," Science **305**, 1007–1009 (2004).
18. C. Dunsby, "Optically sectioned imaging by oblique plane microscopy," Opt. Express **16**, 20306–20316 (2008).
19. A. R. Lyon, C. Dunsby, D. Wilding, K. T. MacLeod, M. B. Sikkel, and S. Kumar, "Application of oblique plane microscopy to high speed live cell imaging," Proc. SPIE **8086**, 80860V (2011).
20. S. Kumar, D. Wilding, M. B. Sikkel, A. R. Lyon, K. T. MacLeod, and C. Dunsby, "High-speed 2D and 3D fluorescence microscopy of cardiac myocytes," Opt. Express **19**, 13839–13847 (2011).
21. M. B. Bouchard, V. Voleti, C. S. S. Mendes, C. Lacefield, W. B. Grueber, R. S. Mann, R. M. Bruno, and E. M. C. Hillman, "Swept confocally-aligned planar excitation (SCAPE) microscopy for high-speed volumetric imaging of behaving organisms," Nat. Photonics **9**, 113–119 (2015).
22. M. B. Sikkel, S. Kumar, V. Maioli, C. Rowlands, F. Gordon, S. E. Harding, A. R. Lyon, K. T. MacLeod, and C. Dunsby, "High speed sCMOS-based oblique plane microscopy applied to the study of calcium dynamics in cardiac myocytes," J. Biophoton. **9**, 311–323 (2016).
23. B. Huang, D. Xie, and R. Mcgorty, "High-NA open-top selective-plane illumination microscopy for biological imaging," Opt. Express **25**, 17798–17810 (2017).
24. Y. Shin, D. Kim, and H.-S. Kwon, "Oblique scanning 2-photon light-sheet fluorescence microscopy for rapid volumetric imaging," J. Biophoton. **11**, e201700270 (2018).
25. M. Kumar, S. Kishore, J. Nasenbeny, D. L. McLean, and Y. Kozorovitskiy, "Integrated one-and two-photon scanned oblique plane illumination (sopi) microscopy for rapid volumetric imaging," Opt. Express **26**, 13027–13041 (2018).
26. M. Kumar and Y. Kozorovitskiy, "Tilt-invariant scanned oblique plane illumination microscopy for large-scale volumetric imaging," Opt. Lett. **44**, 1706–1709 (2019).
27. R. D. Vaadia, W. Li, V. Voleti, A. Singhania, E. M. C. Hillman, and W. B. Grueber, "Characterization of proprioceptive system dynamics in behaving Drosophila larvae using high-speed volumetric microscopy," Curr. Biol. **29**, 935–944 (2019).
28. E. J. Botcherby, R. Juškaitis, M. J. Booth, and T. Wilson, "An optical technique for remote focusing in microscopy," Opt. Commun. **281**, 880–887 (2008).
29. A. W. Lohmann, "Scaling laws for lens systems," Appl. Opt. **28**, 4996–4998 (1989).
30. S. J. Drake, "Systems and methods for forming an image of a specimen at an oblique viewing angle," PCT Patent WO2003027644A1 (April3, 2003).

E Curriculum Vitae

Mein Lebenslauf wird aus datenschutzrechtlichen Gründen in der elektronischen Version meiner Arbeit nicht veröffentlicht.

F List of Publications

Publikationsliste

1. Prevedel, R., Yoon, Y.-G., Hoffmann, M., Pak, N., Wetzstein, G., Kato, S., et al. (2014). Simultaneous whole-animal 3D imaging of neuronal activity using light-field microscopy. *Nature Methods*, *11*(7), 727–730.

2. Reiten, I., Uslu, F. E., Fore, S., Pelgrims, R., Ringers, C., Verdugo, C. D., et al. (2017). Motile-cilia-mediated flow improves sensitivity and temporal resolution of olfactory computations. *Current Biology*, *27*(2), 166–174.

3. Hoffmann, Maximilian, Papadopoulos, I. N., & Judkewitz, B. (2018). Kilohertz binary phase modulator for pulsed laser sources using a digital micromirror device. *Optics Letters*, *43*(1), 22–25.

4. Hoffmann, Maximilian, & Judkewitz, B. (2019). Diffractive oblique plane microscopy. *Optica*, *6*(9), 1166–1170.

5. Horstmeyer, R., Hoffmann, M., Ruan, H., Judkewitz, B., & Yang, C. (2020). Imaging Deep in the Brain with Wavefront Engineering. *Handbook of Neurophotonics*, 147

Impact factors of the publications stated as required by Charité regulations: 1: 21.60 , 2: 9.25 , 3: 3.7 , 4: 13.94 , 5: -

G Acknowledgments

I would like to thank:

Benjamin Judkewitz Johannes Anand Caroline Berlage Thomas Chaigne Georg Changsheng Liu Verity Cook Diego Di Battista Lena Dressler Ana Faustino Antonia Groneberg Nahid Hakiy Jörg Henninger Roarke Hoarstmeyer Myola Kadonianskyi Tobias Leva Daniil Markov Ioannis Papadopoulos Lisanne Schulze Edit Szügyi Malinda Tantirigama Anne Wrana Staff of Charité Facility Management Staff of Research Institutes for Experimental Medicine Charité Staff of the Scientific Laboratories Center Charité Staff of the MedNeuro Graduateschool